Chapter 3

Neutron Induced Reaction Cross-sections for Structural Materials

In this chapter, we present the measurements of neutron induced cross-sections of $^{159}Tb(n,\gamma)^{160}Tb$, $^{113}In(n,n')^{113m}In$, $^{115}In(n,2n)^{114m}In$, $^{115}In(n,n')^{115m}In$ reactions using quasi-mono-energetic neutrons generated by $^{7}Li(p,n)$ reaction. This present chapter also provides the measurement of $^{181}Ta(n,2n)^{180}Ta$ reaction cross-section at 14.78 MeV neutron energy generated by $^{3}H(^{2}H,n)^{4}He$ reaction. The experiments were performed at 14UD Bhabha Atomic Research Center-Tata Institute of Fundamental Research (BARC-TIFR) Pelletron accelerator at TIFR and Purnima Accelerator at Nuclear Physics Division, BARC, Mumbai, India. The measurements have been performed, using neutron activation technique followed by off-line γ-spectroscopy. The reaction cross-sections formulations have been provided along with comprehensive discussion of the uncertainty analysis by adopting the ratio measurement technique. The section 3.8 provide a deep understanding about the measurement and basic knowledge, which would be give better understanding about the sub-sections 3.7.1 and 3.7.2 subsections. TALYS code was used with the ENDF/B-VII.1, JENDL-4.0, and JEFF-3.3 evaluated data libraries to compare the present results. The results of this chapter are of significantly importance significant important for reactor structural materials and advancement of reactor technology. The results also highlight the relative measurement of reaction cross-sections up to 20 MeV incident proton energies by applying the low-energy tailing correction.

The work from this chapter has been published in the following journal

(1) **B. K. Soni**, Rajnikant Makwana, S. Mukherjee, Siddharth Parashari, S.V. Suryanarayana, B.K. Nayak, H. Naik, M. Mehta, Neutron capture cross-sections for ^{159}Tb isotope in the energy range of 5 to 17 MeV, Applied Radiation and Isotopes, 141 (2018) 10-14.

(2) **Bhargav Soni**, Siddharth Parashari, S. Mukherjee, Rajnikant Makwana, S. V. Suryanarayana, B. K. Nayak, H. Naik, J. Varmuza, K. Katovsky, Measurement of the ^{nat}In(n,γ)^{116m}In reaction cross-section at the neutron energies of 10-20 MeV, Eur. Phys. J. Plus, 135, (2020) 300.

(3) **Bhargav K. Soni**, Siddharth Parashari, S Mukherjee, Rajnikant Makwana, M Mehta, R Chauhan, S V Suryanarayana, I Pasha, L S Danu, H Naik, B K Nayak, J Varmuza and K Katovsky, Measurements of ^{181}Ta(n,2n)^{180}Ta reaction cross-section at the neutron energy of 14.78 MeV, Indian Journal of Pure & Applied Physics, 58, (2020) 228-233.

3.1 Introduction

Extensive work has been carried out over the years in order to make nuclear energy more efficient and to reduce the production of long-lived actinides. A solution is to convert long-lived radioisotopes into short-lived isotopes which can then decay safe radiation limit for safer handling of the nuclear waste/residues. Other solution is, to use an alternative fuel which would produce energy efficiently and generate considerabely less production of radioisotopes with relatively longer half-life. ADSs[1] [1–8] may provide both, the solutions together as it can be used in a reactor producing efficient green energy and on the other hand, it can also be used for the transmutation of long-lived isotopes into short ones [1–4].

A considerable amount of work has also been carried out to understand the behavior of different materials in extreme environment of a nuclear reactor. Different metals/alloys have different properties that make them suitable to be used in the structural components of a reactor, which are able to withstand the high radiation dose coming from a reactor core.

Terbium (Tb) is of great importance for the reactor technology and nuclear model development because it works as a venom in fission product. Tb is commonly found as a rare-earth impurity in structural materials [9] and some isotopes which are widely used in nuclear medicine, like ^{149}Tb and ^{161}Tb are used in cancer treatment, ^{149}Tb and ^{152}Tb are used in Positron Emission Tomography (PET), while ^{155}Tb is used in Single Photon Emission Computed Tomography (SPECT). A nuclear reactor produces different high energy particles like α, β, γ and neutrons during its operation. These particles irradiate the surrounding materials and produce radioactivity and hence damages the inner reactor core assembly. Therefore, the reaction cross-section data for all these materials becomes vital for all possible neutron energies [9]. On the other hand, the knowledge of neutron capture cross-sections is also crucial for the design of the fast reactors and to improve the reactors which are currently in use. Hence, it is necessary to measure the experimental nuclear data in the neutron energy range from thermal to the maximum available neutron energies.

Indium (In) and gold (Au) have also been extensively used in the flux measurement for the neutron-induced reactions. The neutron capture cross-sections of In have been studied for the refinement of control rods used in pressurized water reactor (PWR). These control rods are made up of silver, indium and cadmium which are used to capture fast neutrons produced from the reactor core [10]. Indium occurs naturally as two stable isotopes, ^{113}In and ^{115}In, having abundances of 4.29 and 95.71%, respectively. The (n, n') reaction of ^{115}In isotope has negligible threshold and has a significantly higher cross-section compared to other elements in periodic table. It is widely used in the measurement of neutron spectra obtained from both the fusion and fission reactors [11]. Similarly, the $(n, 2n)$

---

[1]A brief discussion on ADSs is provided in section 1.1.1

reaction channel has longer half-life and higher cross-sectional value, which is useful in the activation studies and dosimetry applications [12]. Therefore, In is an important element for neutron flux measurements; hence, the cross-sectional measurements are required to be carried out with better precision.

Tantalum (Ta) is regarded as a control-rod material for lead-bismuth cooled fast reactors. Moreover, neutron-induced activation cross-sections of Tantalum are needed [13] for the decommissioning of light-water reactors [14]. Also, it is very crucial for both nuclear fission and fusion applications. It has a major constituent of the low activation ferritic-martensitic steel Eurofer which is qualified for future fusion reactors, based on the test irradiations in the International Fusion Irradiation Facility (IFMIF). Hence, Tantalum is candidate material of the spallation target [15] to be used for accelerator driven subcritical systems (ADSs).

In addition to ADSs, ITER[2] [16] is also being developed to produce even more efficient energy without producing any hazardous radiochemical waste. ITER can address the issue of waste disposal and energy requirement at once. The scattered radiation from an operational ITER may cause radiation damage to the surrounding materials, as already discussed in section 1.1.2. The toroidal coils of ITER confines the plasma within the reactor core, to achieve the maximum irradiation from neutrons, high energy protons and α-particles. The coils are made of Nb_3Sn, a superconducting material to make high magnetic field to hold the plasma inside the core [17]. Tin (Sn) being used in the coils, becomes important to study for neutron reaction channels to estimate safety and secondary particle production rates.

Taking this into consideration, neutron induced reaction cross-sections were measured for ^{159}Tb [18], $^{113,115}In$ [19] and ^{181}Ta [20] from quasi-monoenergetic neutrons, produced by $^{nat}Li(p,n)$ and $^{3}H(^{2}H,n)$ reactions for incident neutron energies up to 20 MeV. The reaction cross-sections were measured from the residues by employing off-line γ-ray spectroscopy method followed by neutron activation analysis. The uncertainty and correlation between the present measured data is calculated using the ratio technique of covariance analysis. The present chapter sequentially provides details regarding the particle accelerator used in the measurement, γ-ray spectroscopy, mathematical description of the reaction cross-section and covariance analysis, the neutron irradiation experiment with neutron flux measurement, corrections applied in flux calculations. At-last, the calculations are provided for individual measurement and detailed discussion of the excitation functions.

---

[2]A brief discussion about ITER devices is given in section 1.1.2

3.2 Particle Accelerators used for the Irradiation

3.2.1 14UD Pelletron Accelerator

The 14UD pelletron accelerator has been incepted in 1989 at Bhabha Atomic Research Centre-Tata Institute of Fundamental Research (BARC-TIFR) Mumbai, India. Pelletron is a Tandem Van-de-Graff type electrostatic accelerator, which is housed inside a tank about 6 m in diameter and 25 m long. The accelerator tank is filled with a highly insulating gas SF_6 at 80-100 pressure. The purpose behind using SF_6 gas is to provide an insulation between high voltage terminals and to prevent arching between the accelerator the wall of the tank. A typical schematic diagram of the accelerator is shown Figure 3.1.
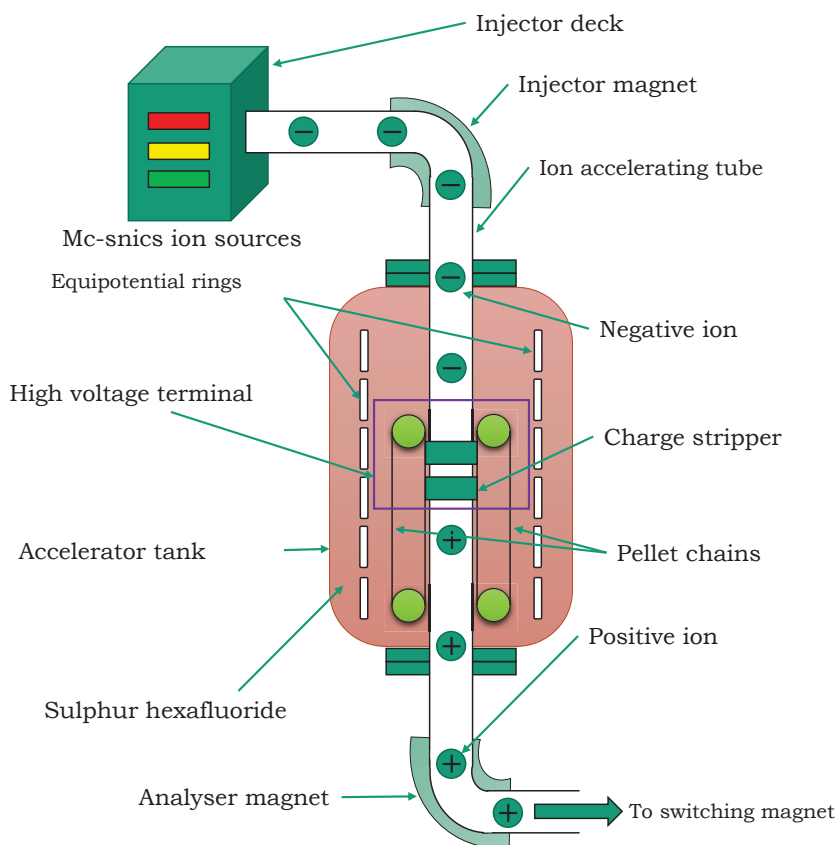

Figure 3.1: A schematic diagram of 14UD Pelletron Accelerator installed at BARC-TIFR Facility.

The injector deck is located at 40 m elevation in accelerator tower. Which consists of high voltage deck (300 kV), ion source, pre-accelerating tube and injector magnet. In which a Cesium sputter ion-source is used to generate negative ions from a selected source, which are further accelerated upto ≈ 300

keV. These negatively charged particles are accelerated to small energies in pre-accelerating tube followed by injection into the main beam line of the pelletron via injector magnet. The beam is further accelerated towards the center of the tank, where the high potential terminal V_t is situated which increases the energy of ions up to qV_t. The charge is continuously transferred to the terminal by a rotating chain of steel pellets, which helping in achieving the high electric potential at the terminal. Inside the terminal, the ions are made to pass through a thin carbon foil or a small volume of a gas, where they loose electrons and become highly positive. Now due to continuous charge collection at the higher positive terminal the positive ions start to repel from the terminal, and further accelerate to the bottom of the tank which is at the ground potential. Lastly, with the help of switching magnets the accelerated ion-beam can be guided to the suitable beam-lines at the main beam hall of the BARC-TIFR facility.

If 'q' is the charge state of the positive ions after passing through the stripper, then the qV_t energy is gained by ions during the acceleration to the ground potential the tank. Hence, the energy gain by the ion beam through acceleration can be given by,

$$E = E_0 + (q + 1)V_t$$

Where, E_0 is the energy of accelerated ions and q is the charge state after stripping [21].

3.2.2 Purnima Neutron Generator

The Purnima neutron generator facility is situated at Neutron & X-Ray Physics Division, BARC, Mumbai, India. Which is a Cockcroft Walten type multiplier 300 kV electrostatic DC accelerator [22]. The D^+ ions were used to produced a suitable energy of neutrons. Where the D^+ ions from the inductively coupled radio frequency ion source, which is accelerated to 300 kV. These extracted ions were further focused using Einzel lens and impinged onto titanium-tritium (TiT) target with copper backing plate to generate 14.1 MeV neutrons through the below reaction,

$$^2H + {}^3H \longrightarrow {}^4He + {}^1n + 17.6\,\text{MeV}, E_n = 14.1\,\text{MeV}$$
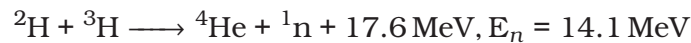
Neutron generator has water cooled with a replaceable target assembly to accommodate 25-47 mm diameter target. Due to the beam power dissipation in TiT the system was cooled with chilled water passing around target [23]. Here the production of neutron can be controlled by two parameters acceleration voltage and RF ion source. The neutron yield can be operated in both continuous and pulse mode. The entire operation is controlled by PLC based control unit from outside the neutron generator hall.

The Figure 3.2 shows the photograph of Purnima neutron generator [23, 24].

Figure 3.2: A pictorial view of BARC-Purnima neutron generator facility [23, 24].

For the present work, both the accelerators have been used to produced neutron beams at different projectile energies. The neutrons were generated by using $^7Li(p,n)$ reaction with 8-22 MeV proton beams from pelletron and monoenergitic neutrons (14.78 MeV) by using DT reactions from PURNIMA accelerator. A detailed discussion of the experimental setup for neutron induced reactions are provided in the upcoming subsection 3.8.

3.3 Target Details

In order to analyze samples using activation analysis technique, the target geometry plays an important role. In the present work, self-supporting metal foils of natural occurring isotopes were used for the neutron irradiation. The area of the target (samples and monitor) foils was kept same (1×1 cm^2), this helps in avoiding the area corrections in neutron flux calculations. Each target foils which were used in the irradiation was separately wrapped in thin aluminum (Al) foil (≈ 0.0015 mm). This can prevent the cross-contamination during the irradiation of the targets. Also, the natural lithium (Li) foil was used to generate neutrons via $^7Li(p,n)$ reaction at 14 UD pelletron accelerator. This natural lithium foil of thickness $\approx$3.2 mg/cm^2, was sandwiched between two tantalum (Ta) foils of different thickness for mechanical support. The tantalum foil facing the proton beam allows the protons to interact with lithium foil, and the other tantalum foil stops the protons, which have not interacted with lithium. The TiT target (with copper backing) was used to generate neutrons via DT reaction at Purnima accelerator [22]. The necessary target/monitor details which were used for the
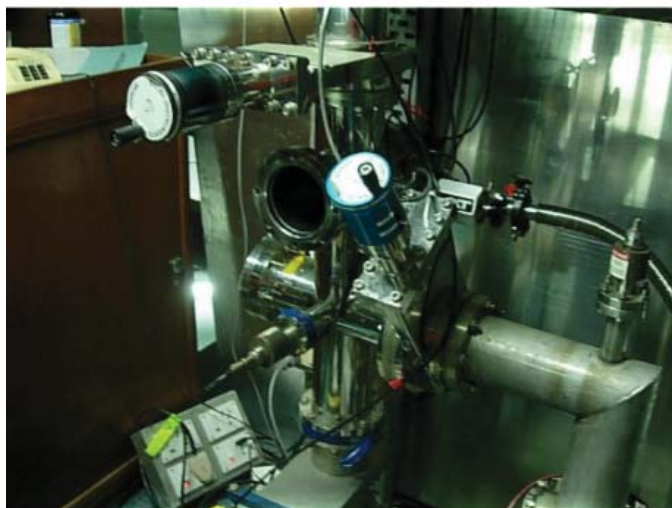
Figure 3.3: A pictorial view of the 6 meter irradiation setup at BARC-TIFR Pelletron accelerator [21].

measurement of neuron-induced reaction cross-sections are given in Table 3.1. A pictorial view of the geometry of 6 meter irradiation setup is shown in Figure 3.3.

3.4 γ-ray Spectroscopy

In the present work, the off-line γ-ray technique has been employed to measure the activities produced in the irradiated samples [25, 26]. After the irradiation has been completed, the delayed γ-rays emerging from the irradiated samples are recorded using a pre-calibrated HPGe detector. The method is user-friendly which gives freedom to record the γ-ray spectrum of the sample for a significant amount of time, by which users reduce the statistical uncertainty in the measurement. This technique also allows the user to record the spectrum with the half-life ($T_{1/2}$) of residues in focus. Although this method has a disadvantage that the reaction cross-sections of residues which possess shorter half-lives of the order of few seconds cannot be recorded. A Brief description of the HPGe detector used in the current work is given below

3.4.1 High Purity Germanium Detectors

HPGE detector is a semiconductor type detector, widely used for the on-line/off-line γ-ray/X-ray spectroscopy [27]. When a γ-ray enters the active material of the detector, it ionizes the atoms and produces a number of electron-hole pairs along its path. By applying external electric field the generated electron-hole pair are collected across the boundaries of the active volume of detector. The collected signal is proportional to the deposited energy which is further it converted by the electronics of the detector to a spectrum. A large current flows during

Table 3.1: Target details for the neutron induced reaction cross-section measurements.

Set.[†] No.	Samples	Incident E_P (MeV)	Area (cm^2)	Thickness (mm)	Weight (mg)
1.	Sample ^{nat}Tb	7			32.3
2.		15	1×1	0.1	33.3
3.		18.8			36.3
1.	Monitor ^{232}Th	7			201.1
2.		15	1×1	0.1	190.2
3.		18.8			211.1
1.	Sample ^{nat}In	13			243.1
2.		16	1×1	0.1	186.0
3.		19			181.0
4.		22			239.0
1.	Monitor ^{nat}Al	13			
2.		16	1×1	0.1	≈ 33.0
3.		19			
4.		22			
1.	Sample $^{nat}Ta^b$	14.78	1×1	0.025	239.1
1.	Monitor $^{nat}Au^b$	14.78	1×1	0.025	334.3

[†]here set represent samples with their corresponding monitors
[a]used as sample/monitor at 14UD Pelletron accelerator
[b]used as sample/monitor at Purnima Neutron Generator

forward biased operation due to the thermal excitation of atoms. However, a the negligible current flows during reverse biased operation, such that; the current due to the ionizing radiation can be detected. Compared to the forward bias, in reverse bias condition the width of the depletion region is large, hence, generally semiconductor detectors are operated in reversed bias. A schematic diagram of a HPGe detector is shown in Figure 3.4 [28].

A large sensitive volume area of the germanium detector benefits to completely absorb γ-rays up to a few MeV. The hyper-pure germanium detectors or high-purity germanium detectors (HPGe) were manufactured by the purification techniques which remove the impurities in the germanium crystal. Basically the impurity of the crystal decrease the performance of the detector by traping electrons and holes in the crystal. For better performance and efficiency, intrinsic region is created in the germanium crystal by doping it with lithium ions (Ge(Li)), this helps electrons and holes to reach the contacts and to produce a signal.
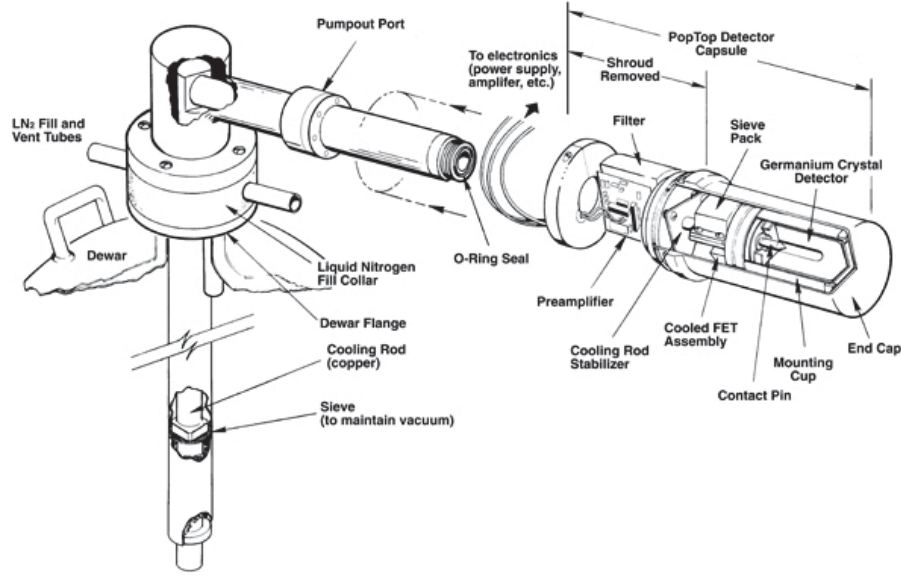
Figure 3.4: Schematics of a typical HPGe detector connected to a cooling dewar [28]

3.4.2 Detector Efficiency and Energy Calibration

For activation analysis technique a proper energy calibration of the high resolution detector is essential to identify the characteristic γ-rays of populated residues. Therefore, in present measurements, a ^{152}Eu point source of known strength was used for the HPGe detector calibration. The γ-rays emitted from the ^{152}Eu point source [29] covers broad energies from 122 keV to about 1408 keV. The prominent γ-rays that are utilized in the calibration of detector along with their intensities as listed in Table 3.2 and characteristic γ-ray energy spectrum of ^{152}Eu observed is displayed in Figure 3.5.

The resolution of both the HPGe detector systems[3] were measured to be ≈ 1.8 keV for 1332.50 keV γ-ray of ^{60}Co. The HPGe detectors were coupled with PC-based 4096 multichannel channel analyzer. Different γ-ray acquisition softwares like, MAESTRO [30], Genie [31] LAMPS [32], and FitzPeaks [33] were used for the recording and analysis of different spectra.

3.4.3 Efficiency of the Detector

^{152}Eu source has been used to determine the efficiency of the HPGe detector. For each γ-ray energy, the photopeak efficiency ε_G is geometry independent, although, their absolute value depends on the detector geometry and determined from the following equation,

$$\varepsilon_G = K_c \frac{C_{obs}}{A_0 I_\gamma e^{-\lambda T} \triangle t} \tag{3.1}$$

where, K_c is the summing correction factor for the coincidence-summing effect

---

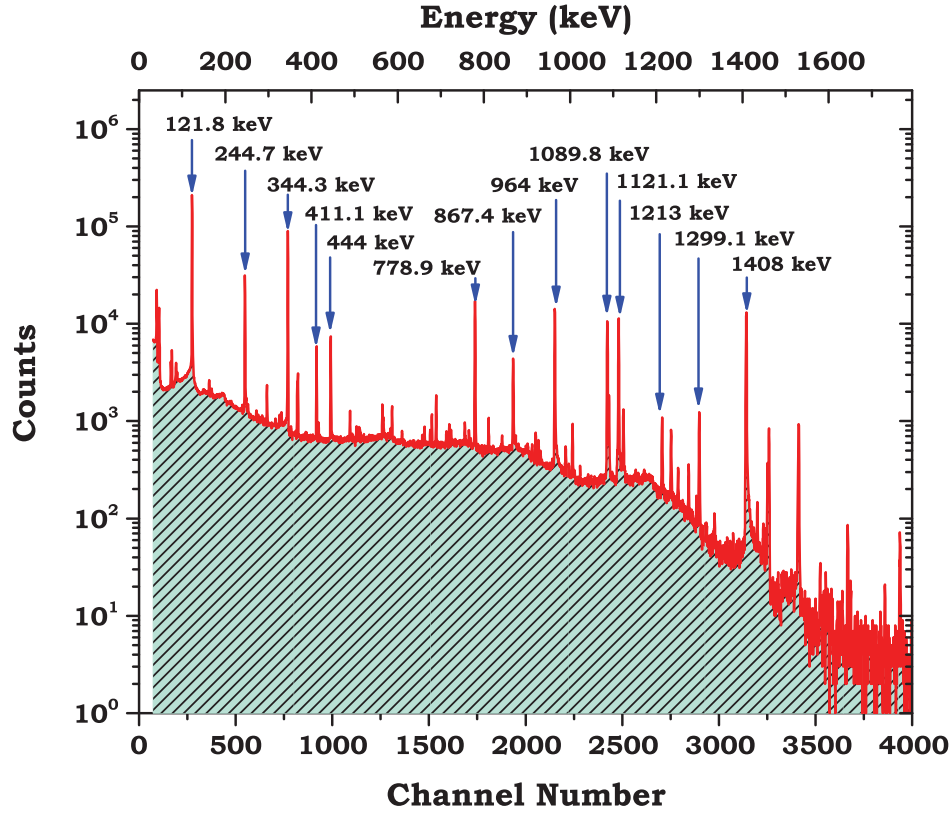[3]One at Pelletron and another at Purnima setup.

Figure 3.5: A typical recorded spectrum of a standard ^{152}Eu γ-ray source denoted with prominent γ-lines

[34]. The coincidence summing correction was calculated using the EFFTRAN code [35] for individual γ-lines, C_{obs} is the number of counts detected for the γ-line of interest during time interval △t, A_0 is the activity of ^{152}Eu γ-ray source at the time of production of the source, I_γ is the absolute intensity [29] of the appropriate γ-ray, λ is the decay constant, and T is the hiatus between the dates of production and observation.

The typical (source-detector) arrangement which was used for the γ-ray counting measurement at 14UD Pelletron facility and Purnima are shown in Figure 3.6 and 3.7 [21].

The typical geometry dependent efficiency (ε_G) as a function of γ-ray energies (E_γ) for Pelletron as well as for Purnima experiments at different distances from the detector end cap are shown in Figure 3.8.

The efficiencies which are used for the analysis of the $^{159}Tb(n,\gamma)^{160}Tb$, $^{113}In(n,n')$ ^{113m}In, $^{115}In(n,2n)^{114m}In$, $^{115}In(n,n')^{115m}In$ reaction cross-sections are shown in Figure 3.8 (A), whereas, the efficiencies used for the $^{181}Ta(n,2n)^{180}Ta$ reaction are presented in Figure 3.8 (B).

A fourth order polynomial was used to get the best fit for the energy dependent efficiency curves which is described as follows,

Table 3.2: Listed γ-rays along with their absolute intensities (%) for the ^{152}Eu source.

Sr. No.	γ-ray Energy (keV)	Absolute Intensity ($I_\gamma(\%)$)
1	121.8	28.6
2	244.7	7.6
3	344.3	26.5
4	411.1	2.2
5	444.0	2.8
6	778.9	12.9
7	867.4	4.2
8	964.1	14.2
9	1085.9	10.2
10	1089.7	1.7
11	1112.1	13.6
12	1213.0	1.4
13	1299.1	1.6
14	1408.0	21.0

Figure 3.6: Pictorial view of typical source-detector counting setup at 14 UD Pelletron facility

$$G = aE_0 + bE_1 + cE_2 + dE_3 + eE_4 \tag{3.2}$$

Where a, b, c, d, and e are the constants with values relying on the distance between the source and the detector. The value of these can be determined by applying the least square fit and E is the energy of the characteristic γ-ray.

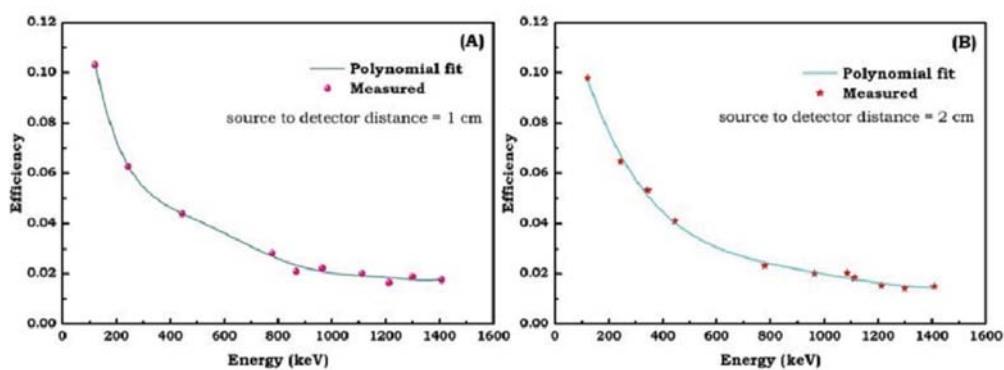**Figure 3.7:** Pictorial view of a typical detector setup used at Purnima

Figure 3.8: Measured efficiencies for the detector used for (A) the $^{159}Tb(n,\gamma)^{160}Tb$, $^{113}In(n,n')^{113m}In$, $^{115}In(n,2n)^{114m}In$, $^{115}In(n,n')^{115m}In$ reaction cross-sections at Pelletron BARC-TIFR, (B) $^{181}Ta(n,2n)^{180}Ta$ reaction at Purnima, BARC,

3.5 Residues Identification

Interaction of projectile with target nucleus populate reaction residues. Each has a different decay mode, γ-line and their intensities which provides the basic information about the specific evaporation residue. The γ-ray activities induced in the target foils during the irradiation have been counted at increasing time intervals following the half-lives ($T_{1/2}$) of the residues under consideration. In case of intermixing of γ-rays due to different isotopes, the contribution of each residue can be separated out by recording the induced activity for a considerably longer time [36]. The spectroscopic properties like; half-life, characteristic γ-ray, branching ratio and spin for the identified residue were taken from NuDat database [29].

The general details regarding the experimental method and steps are provided in the upcoming sections. Specific details with a rigorous discussion about the neutron production and the stacks used in neutron activation are provided in the subsection 3.8, followed by the complete discussion on the measurement of the reaction cross-sections.

3.6 Mathematical Description of the Reaction Cross-Section

The occurrence of various nuclear reactions, in general, take place when the sample is irradiated with a beam of particles. Through these various interactions a compound nucleus may be populated, which further decays leaving behind reaction residues with the ejection of various particles such as, proton, neutron, γ, α etc. The residual nuclei thus populated are in their excited states. The excited residual nuclei may come to ground state by emitting their characteristic γ-ray. Initially, the number of populated residues during the activation need to be quantified. Let N_0 is the number of nuclei available in the target, ϕ is the flux of neutrons and the activation cross-section of the target nuclei through a particular reaction channel define as σ_R, then the activation rate can be determined according to the following equation [21],

$$N = N_0 \phi \sigma_R \tag{3.3}$$

The disintegration rate of the produced radioactive nuclei still alive at the end of the irradiation can be given by,

$$\left(\frac{dN}{dt}\right)_t = N exp(-\lambda t_w)[1 - exp(-\lambda t_i)] \tag{3.4}$$

where t_i is the time period, when the target got irradiated by a beam with steady current, the cooling time after the irradiation stops is denoted by t_w and radioactive decay constant of the nucleide λ is the radioactive decay constant of

the residual nuclei. This decay constant is related to the half-life ($T_{1/2}$) as follows,

$$\lambda = \frac{0.693}{T_{1/2}} \tag{3.5}$$

The last exponential term in the equation 3.4 accounts for the saturation correction. It should also be considered that constant beam current condition during the irradiation is not accomplished, i.e. the residue half-life is shorter than the irradiation time period (t_i). Thus, the number of radioactive nuclei which decay due to their short half-life accomplished by small time interval dt can be given by;

$$dN = N exp(-\lambda t_w)[1 - exp(-\lambda t_i)]dt \tag{3.6}$$

Let $\triangle t$ be the time to record the induced activity from the activated sample, then the emitted total number of nuclei in the time t_w to $t_w + \triangle t$ is given by;

$$C = \int_{t_w}^{t_w + \triangle t} dN \tag{3.7}$$

$$C = N[1 - exp(-\lambda t_i)] \int_{t_w}^{t_w + \triangle t} exp(-\lambda t_w)dt \tag{3.8}$$

$$C = N\frac{[1 - exp(-\lambda t_i)][1 - exp(-\lambda \triangle t)]}{\lambda exp(\lambda t_w)} \tag{3.9}$$

If the activity of irradiated sample is measured by a suitable γ-ray spectrometer having geometry dependent efficiency (ε_G), then the relation of the absolute counting rate 'C' is describe as [21],

$$C = \frac{C_{obs}}{(\varepsilon_G)I_\gamma} \tag{3.10}$$

where, I_γ is the branching intensity of the characteristic γ-ray [29]. Thus, the equation 3.3 can be rewritten for the reaction cross-section σ_R at a given energy E as,

$$\sigma_R = \frac{C_{obs}\lambda}{N_0\phi\varepsilon_G I_\gamma[1 - exp(-\lambda t_i)][1 - exp(-\lambda \triangle t)]exp(\lambda t_w)} \tag{3.11}$$

where, C_{obs} is the measured counts under the photo-peak of the characteristic γ-ray.

The above equation 3.11 can be used in the measurement of the reaction cross-sections of a residue at a given energy. Furthermore, this equation can be slightly modified in-terms of the counting time of the detector (T_R) and the live time of counting (T_L) because of the dead time of the detector. The modification in equation 3.11 is given as,

$$\sigma_R = \frac{C_{obs}\lambda(T_R/T_L)}{N_0\phi\varepsilon_G I_\gamma K[1 - e^{-\lambda t_i}]e^{-\lambda t_w}[1 - e^{-\lambda T_L}]} \tag{3.12}$$

where, C_{obs} is the number of counts for corresponding γ-ray from monitor reaction, λ is the decay constant ($\lambda = 0.693/t_{1/2}$), T_R and T_L are the clock time and live time measured during the counting of the spectrum, I_γ is the branching intensity of the respective γ-ray taken from Ref. [29], N_0 is the number of target nuclei available in the sample and ϵ is the detector efficiency for the chosen γ-ray. Above formulation can be used for calculating the cross-section produced from the populated reaction residue.

In the present study we have examined the neutron induced reactions. For this purpose, the neutron flux cannot be estimated by direct method. Therefore, a monitor reaction was incorporated in the neutron cross-section measurements. Basically this relative method is useful in the neutron induced reaction cross-section measurements where the accurate flux estimation is required. The neutron flux ($< \Phi >$) is given as,

$$< \Phi >=< \sigma_W > \frac{C_{obs}\lambda(T_R/T_L)}{N_0\varepsilon_G I_\gamma K[1 - exp(-\lambda t_i)]exp(-\lambda t_w)[1 - exp(-\lambda T_L)]} \tag{3.13}$$

where, $< \sigma_W >$ is the weighted average cross-section for the monitor reaction and rest of the quantities have their usual meanings as in equation 3.12. The spectral average cross-section for monitor reaction $< \sigma_W >$ can be given by using the following expression,

$$< \sigma_W >= \frac{\int_{E_i} \phi_{E_i}\sigma_{E_i}}{\int_{E_i} \phi_{E_i}} \tag{3.14}$$

Therefore, the neutron-induced reaction cross-section σ_R can now be further modified with by using equations 3.12 and 3.13 as,

$$\sigma_R = \frac{C_{obs}\lambda(T_R/T_L)}{N_0 < \Phi > \varepsilon_G I_\gamma K[1 - e^{-\lambda t_i}][e^{-\lambda t_w}][1 - e^{-\lambda T_L}]} \tag{3.15}$$

This indirect method of calculating the neutron flux for the measurement of reaction cross-section may give large uncertainties and correlations between the different attributes. Hence, the uncertainty in measured data of the neutron induced reaction cross-section have been calculated using co-variance analysis [37, 38]. The analysis has been widely used and proposed for examination of the uncertainties in the data. The co-variance analysis technique has been described in detail in the following section.

3.7 Uncertainty Propagation using Covariance Analysis

The quality of the data is not only determined by the values measured, but also by their uncertainties. We need to know (ideally) all the possible sources of uncertainties in our experiment and data processing stage. However, the

knowledge itself is not enough, we need also to understand where and how the uncertainties propagate.

The covariance (correlation) analysis [38] is a statistical and mathematical tool based on the error estimation by predicting means and covariances in non-linear systems. Covariance analysis provides the best estimation of the uncertainty along with the cross-correlations among the measured quantities, which in this case, are the reaction cross-sections. Apart from the counting statistics from a spectrum, other quantities like, the γ-abundances, efficiency of detector, flux, half-life of residues, etc, are taken from different sources which probably contains significant errors.

The method is based on the assumption that the result of an observation can be considered as a random variable $x = (x_1, x_2, x_3, ..., x_n)$. The normalization condition of the probability distribution $p(x)$ of x can be given as, $\int_{-\infty}^{+\infty} p(x)dx = 1$, where $dx = dx_1 dx_2 dx_3...dx_n$. The expectation value 'A' of a real-valued function $f(x)$ can be defined as [21],

$$A(f(x)) = \int_{-\infty}^{+\infty} f(x)p(x)dx \qquad (3.16)$$

the mean and variance of variable x_k are given by,

$$\tilde{\mathbf{x}}_\mathbf{k} = A(x_k); \quad \mathbf{Var}(x_k) = A[(x_k - \tilde{x}_k)^2] \qquad (3.17)$$

Since, the variables are dependent, therefore, the covariance and the correlation among the variables x_k are defined as [38],

$$\mathbf{Cov}(x_k, x_i) = \int (x_k - \tilde{x}_k)(x_i - \tilde{x}_i)p(x_1, x_2...x_n)dx \qquad (3.18)$$

$$\mathbf{Corr}(x_k, x_i) = \frac{Cov(x_k, x_i)}{\sqrt{Var(x_k)}\sqrt{Var(x_i)}} \qquad (3.19)$$

where, $-1 \le \mathbf{Corr}(x_k, x_i) \le 1$ and the uncertainty can be defined as the standard deviation $\triangle x_k = \sqrt{\mathbf{Var}(x_k)}$.

3.7.1 Estimation of Uncertainty in the Detector Efficiency

The geometry dependent efficiency of the HPGe detector is given by the following formula,

$$\varepsilon = K_c \frac{C_{obs}}{A_0 I_\gamma \triangle t e^{-\lambda T}} \qquad (3.20)$$

where, A_0 is the activity of ^{152}Eu γ-ray source at the time of manufacturing, λ is the decay constant, T is the hiatus between the date of manufacturing and the observation, $\triangle t$ is the counting time for the source, I_γ is the intensity of the particular γ-ray, K_c is the summing correction factors for the coincidence-summing effect [39]. Which were calculated using EFFTRAN code [35] and C_{obs} is

the number of counts measured during the time $\triangle t$ in with only counts (C) related to the geometry of the HPGe detector.

Mainly the uncertainty in the detector efficiency are contributed from γ-ray abundance (I_γ), γ-ray counts (C), source activity (A_0), and half-life of radionuclide ($T_{1/2}$). Where the terms t and K_c given in equation 3.20 are determined without uncertainty and in present measurement treated as constants. Therefore, the efficiency of the detector can be written as the function of four variables as,

$$\varepsilon = f(C, A_0, I_\gamma, T_{1/2}) \tag{3.21}$$

the standard deviation in efficiency can be given by considering the Taylor series expansion of equation 3.21 by neglecting the higher order terms [21, 40],

$$\delta\varepsilon = \left(\frac{\partial\varepsilon}{\partial C}\right)\delta C + \left(\frac{\partial\varepsilon}{\partial A_0}\right)\delta A_0 + \left(\frac{\partial\varepsilon}{\partial I_\gamma}\right)\delta I_\gamma + \left(\frac{\partial\varepsilon}{\partial T_{1/2}}\right)\delta T_{1/2} \tag{3.22}$$

Squaring both the sides of equation 3.22 and taking expectation values, we get,

$$
(\triangle\varepsilon)^2 = \left(\frac{\partial\varepsilon}{\partial C}\right)^2(\triangle C)^2 + \left(\frac{\partial\varepsilon}{\partial A_0}\right)^2(\triangle A_0)^2 + \left(\frac{\partial\varepsilon}{\partial I_\gamma}\right)^2(\triangle I_\gamma)^2 + \left(\frac{\partial\varepsilon}{\partial T_{1/2}}\right)^2(\triangle T_{1/2})^2 + 2\left(\frac{\partial\varepsilon}{\partial C}\right)\left(\frac{\partial\varepsilon}{\partial A_0}\right)cov\,(C, A_0)
$$
$$
+ 2\left(\frac{\partial\varepsilon}{\partial C}\right)\left(\frac{\partial\varepsilon}{\partial I_\gamma}\right)cov\,(C, I_\gamma) + 2\left(\frac{\partial\varepsilon}{\partial C}\right)\left(\frac{\partial\varepsilon}{\partial T_{1/2}}\right)cov\,(C, T_{1/2}) + 2\left(\frac{\partial\varepsilon}{\partial A_0}\right)\left(\frac{\partial\varepsilon}{\partial I_\gamma}\right)cov\,(A_0, I_\gamma)
$$
$$
+ 2\left(\frac{\partial\varepsilon}{\partial A_0}\right)\left(\frac{\partial\varepsilon}{\partial T_{1/2}}\right)cov\,(A_0, T_{1/2}) + 2\left(\frac{\partial\varepsilon}{\partial I_\gamma}\right)\left(\frac{\partial\varepsilon}{\partial T_{1/2}}\right)cov\,(I_\gamma, T_{1/2})
$$

The equation above states that, the law of error propagation is a single-valued function and can be used in uncertainty measurements. The equation 3.23 can be written in terms of matrix notation as,

$$
(\triangle\varepsilon)^2 = \begin{bmatrix} \frac{\partial\varepsilon}{\partial C} & \frac{\partial\varepsilon}{\partial A_0} & \frac{\partial\varepsilon}{\partial I_\gamma} & \frac{\partial\varepsilon}{\partial T_{1/2}} \end{bmatrix}
\begin{bmatrix}
(\triangle C)^2 & cov(C, A_0) & cov(C, I_\gamma) & cov(C, T_{1/2}) \\
cov(C, A_0) & (\triangle A_0)^2 & cov(A_0, I_\gamma) & cov(A_0, T_{1/2}) \\
cov(C, I_\gamma) & cov(A_0, I_\gamma) & (\triangle I_\gamma)^2 & cov(I_\gamma, T_{1/2}) \\
cov(C, T_{1/2}) & cov(A_0, T_{1/2}) & cov(I_\gamma, T_{1/2}) & (\triangle T_{1/2})
\end{bmatrix}
\begin{bmatrix}
\frac{\partial\varepsilon}{\partial C} \\
\frac{\partial\varepsilon}{\partial A_0} \\
\frac{\partial\varepsilon}{\partial I_\gamma} \\
\frac{\partial\varepsilon}{\partial T_{1/2}}
\end{bmatrix} \tag{3.23}
$$

The measured four attributes $(C, A_0, I_\gamma, T_{1/2})$ are uncorrelated with each others. Therefore, uncertainty in the detector efficiency can be calculated applying the quadratic sum formula for 'j' number of γ lines as,

$$(\triangle\varepsilon)^2 = \left(\frac{\partial\varepsilon}{\partial C}\right)^2(\triangle C)^2 + \left(\frac{\partial\varepsilon}{\partial A_0}\right)^2(\triangle A_0)^2 + \left(\frac{\partial\varepsilon}{\partial I_\gamma}\right)^2(\triangle I_\gamma)^2 + \left(\frac{\partial\varepsilon}{\partial T_{1/2}}\right)^2(\triangle T_{1/2})^2 \tag{3.24}$$

which can be written as,

$$\left(\frac{\triangle\varepsilon_j}{\varepsilon_j}\right)^2 = \left(\frac{\triangle C_j}{C_j}\right)^2 + \left(\frac{\triangle A_0}{A_0}\right)^2 + \left(\frac{\triangle I_{\gamma_j}}{I_{\gamma_j}}\right)^2 + (t\,\triangle\,\lambda)^2 \tag{3.25}$$

where the uncertainty in decay constant λ is calculated after converting $T_{1/2}$ data into λ as,

$$\triangle \lambda = \frac{0.693 \triangle T_{1/2}}{T_{1/2}^2} \tag{3.26}$$

Moreover, the covariance matrix for 'j' number of measurements is build from the sandwich formula,

$$(V_\varepsilon)_{jk} = \sum_r e_{jl} S_{jkl} e_{kl} \tag{3.27}$$

where S_{jkl} is the micro–correlation amid e_{jl} and e_{kl} due to the *lth* attribute [41]. The micro-correlation amid different attributes have been assigned on the assumptions [37, 42] as follows,

- Suppose the two quantities (say x_1, x_2) can be obtained independently, then the correlation between them, **Corr**(x_1, x_2) = 0 i.e it is uncorrelated, while **Corr**(x_1, x_2) = 1 fully correlated, when they are completely dependent. Apart from these if the situation $0 <$ **Corr**$(x_1, x_2) < 1$ occurs i.e. two quantities are neither completely dependent nor independently [38] [21].

- The measured counts for different γ-lines were measured individually. Hence they are uncorrelated and therefore, S_{jkl} for counts will be an identity matrix of order $j \times j$.

- The γ-abundance (I_γ) for separate γ-lines of ^{152}Eu is a characteristic property of each γ-line and hence they are also taken as uncorrelated.

- The half-life ($T_{1/2}$) of ^{152}Eu will be same for each γ-line during the decay, hence, they are correlated. The S_{jkm} matrix in particular case would be a square matrix of order $j \times j$ with all the elements as 1.

- The activity (A_0) of ^{152}Eu will be same for each γ-line measurement during the measurements, hence, it would be taken as correlated quantity.

Based on the above discussed points the S_{jkl} matrices for attributes C, A_0, I_γ and $T_{1/2}$ will be written as,

$$\begin{pmatrix} 1 & 0 & \cdots & 0 \\ 0 & 1 & \cdots & 0 \\ \vdots & \vdots & \ddots & \vdots \\ 0 & 0 & \cdots & 1 \end{pmatrix} \begin{pmatrix} 1 & 1 & \cdots & 1 \\ 1 & 1 & \cdots & 1 \\ \vdots & \vdots & \ddots & \vdots \\ 1 & 1 & \cdots & 1 \end{pmatrix} \begin{pmatrix} 1 & 0 & \cdots & 0 \\ 0 & 1 & \cdots & 0 \\ \vdots & \vdots & \ddots & \vdots \\ 0 & 0 & \cdots & 1 \end{pmatrix} and \begin{pmatrix} 1 & 1 & \cdots & 1 \\ 1 & 1 & \cdots & 1 \\ \vdots & \vdots & \ddots & \vdots \\ 1 & 1 & \cdots & 1 \end{pmatrix}$$

The γ-rays taken into measurements (say E_i) may be the others from those taken for efficiency calculations, hence, the detector efficiencies for the γ-lines E_i can be determined from the interpolation model as follows [37]

$$ln\varepsilon_j = \sum_n p_n (lnE_j)^{m-1} \tag{3.28}$$

where, p_n is the nth order fitting parameter and E_j are the energy of the γ-lines. The solution of equation 5 can be determined by taking a matrix notation

$$Z \approx AP \tag{3.29}$$

were, Z ($z_j = ln\varepsilon_j$) is a column matrix, and A is the design matrix with elements $A_{jn} = (lnE_j)^{n-1}$. The least squared method can be applied to estimate matrix parameters p_m. The goodness of the fit can be determined by,

$$\chi_n^2 = (Z - AP)'V_z^{-1}(Z - AP) \tag{3.30}$$

The values of parameters p_n can be extracted from normal equation $\partial^2\chi_n/\partial p_n = 0$. It is written as,

$$\hat{P} = V_{\hat{P}}(A'V_z^{-1}Z) \tag{3.31}$$

where the covariance matrix for solution parameters $V_{\hat{P}}$ is given by,

$$V_{\hat{P}} = (A'V_z^{-1}A)^{-1} \tag{3.32}$$

The matrix element V_z can be determined by using the relation,

$$(V_z)_{jk} = \frac{(V_\epsilon)_{jk}}{<\epsilon_j><\epsilon_k>} \tag{3.33}$$

By using the results of above-mentioned calculations, the covariance matrix for the cross-sections can be determined.

Equation 3.28 with fitting parameters can be used to calculate the efficiencies for the γ-lines of the sample and monitor reactions. Then the covariance matrix can be obtained by matrices Z and A for new efficiencies. With the help of the equations,

$$V_{z_{\epsilon_j}} = A'V_{\hat{P}}A \tag{3.34}$$

&

$$V_{\epsilon_{jk}} = \epsilon_j V_{z_{\epsilon_{jk}}} \epsilon_k \tag{3.35}$$

where, $V_{z_{\epsilon_i}}$ and $V_{\epsilon_{ij}}$ are the covariance matrix for the column matrix Z and for the efficiencies of the sample and monitor reaction γ-lines [21], respectively.

3.7.2 Estimation of Uncertainty in the Reaction Cross-section Measurement

The reaction and monitor cross-sections are measured with the help of equations 3.15 and 3.13, respectively. However, the accurate measurement of neutron activation cross-sections, requires an information about the uncertainty present in it. The ratio measurement technique [38] has been adopted for the covariance analysis in activation cross-section measurements. Therefore, equation 3.15 can be rewritten using equation 3.13 as,

$$< \sigma_s > = < \sigma_m > \frac{C_s N_{0_m} \varepsilon_m I_{\gamma_m} f_{\lambda_m}}{C_m N_{0_s} \varepsilon_s I_{\gamma_s} f_{\lambda_s}} \qquad (3.36)$$

Time factor f defined as,

$$f = (1 - e^{-\lambda t_i})(e^{-\lambda t_w})(1 - e^{-\lambda T_L})/\lambda \qquad (3.37)$$

In the equation 3.36, suffix 's' and 'm' stand for the sample reaction and the monitor reaction parameters, respectively. Using the definition conferred in section 3.7.1, the uncertainty in measured cross-section can be written in the quadratic sum formula,

$$\left(\frac{\Delta \sigma_r}{\sigma_r}\right)^2 = \sum_a \left(\frac{\Delta a_r}{a_r}\right)^2 + \sum_a \left(\frac{\Delta a_m}{a_m}\right)^2 + \left(\frac{\Delta \sigma_m}{\sigma_m}\right)^2 \qquad (3.38)$$

where

$$a = a(C, N_0, \varepsilon, I_\gamma, f)$$

The uncertainties in the time factors should be proliferated using the uncertainties in the decay constants as,

$$\left(\frac{\Delta f}{f}\right)^2 = s_{f\lambda}^2 \left(\frac{\Delta \lambda}{\lambda}\right)^2 \qquad (3.39)$$

with the relative sensitivity written as,

$$s_{f\lambda} = \left(\frac{\lambda t_i e^{-\lambda t_i}}{1 - e^{-\lambda t_i}} - \lambda t_w + \frac{\lambda(T_L)e^{-\lambda(T_L)}}{1 - e^{-\lambda(T_L)}} - 1\right) \qquad (3.40)$$

the final covariance matrix for the measured cross-sections can be determined adopting the sandwich formula,

$$(V_\sigma)_{jk} = \sum_r e_{jl} S_{jkl} e_{kl} \qquad (3.41)$$

where S_{jkl} are the micro-correlation matrices. The correlation matrix can be calculated using (V_σ) by following 3.4 and the uncertainty in cross-section can be calculated as the square root of diagonal elements $((V_{\sigma_{jj}})^{1/2})$ of the covariance matrix. Detailed covariance analysis for typically measured $^{113}In(n, n')^{113m}In$, $^{115}In(n, 2n)^{114m}In$, $^{115}In(n, n')^{115m}In$ reactions are provided in Appendix A.

3.8 Experimental Details

The experiments of the neutron induced reaction cross-section measurement for $^{159}Tb(n,\gamma)^{160}Tb$, $^{113}In(n,n')^{113m}In$, $^{115}In(n,2n)^{114m}In$, $^{115}In(n,n')^{115m}In$, and $^{181}Ta(n,2n)^{180}Ta$ have been performed at the BARC-TIFR Pelletron and BARC Purnima [4] accelerators. The standard neutron activation analysis [5] was used for the measurements.

A natural lithium target (^{nat}Li) was used in the generation of the desired energy neutron beams at the BARC-TIFR Pelletron facility situated at Mumbai, India. The irradiation were carried out at the 6 meter port, in which a prepared target/samples were stick to the 6 meter port on tantalum base or can be placed inside a small pot of plastic, situated just below the Ta base. A schematic diagram of irradiation facility at 6 meter port is shown in Figure 3.9.
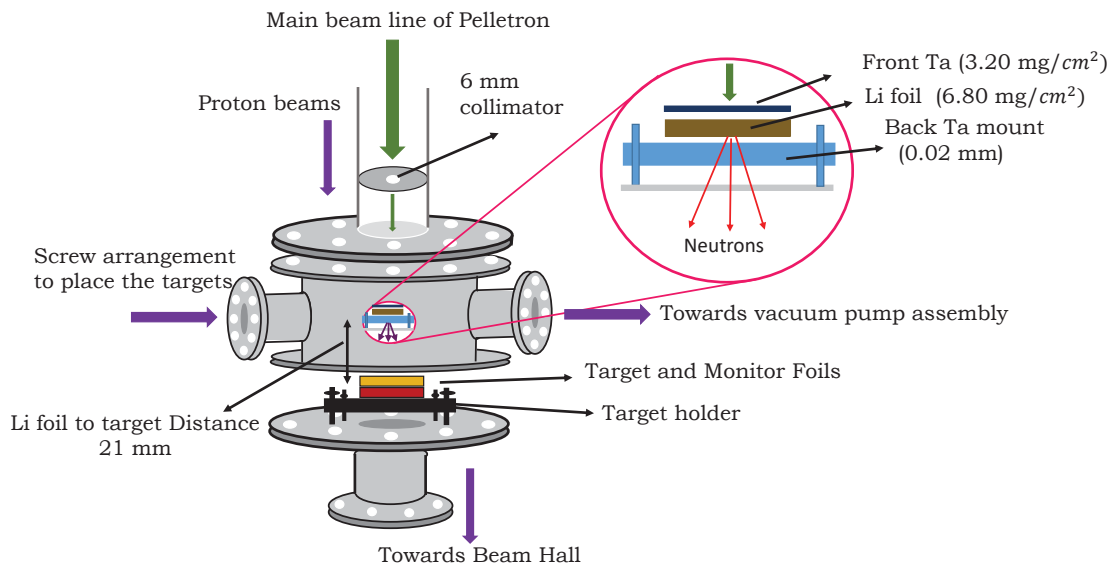
Figure 3.9: A schematic diagram of the target irradiation setup at BARC-TIFR Pelletron with ^{nat}Li metal foil [21].

The natural Li foil is covered with two Ta foils of differing thicknesses on the front and back side. The stack of the Ta-Li-Ta were prepared on the same day of experiment and forthwith mounted at on a platform using screws. Basically this stack was made for the purpose to completely stop the proton beam from the back Ta foil placed at back side of the Li. The neutron beam was generated by bombarding the proton beam of suitable energy from the $^{7}Li(p,n)$ reaction (E_{th} = 1.881 MeV) [43]. Further, these neutron were allowed to interact with on the samples which are placed below the Ta platform, to activate the sample.

A list of experiments performed at the BARC-TIFR Pelletron setup containing different target monitor combination, thicknesses of used Li foils, Ta foils used for the Ta-Li-Ta stack, and the energies of the produced neutron beams are given

---

[4]The details of the Pelletron and Purnima accelerators are given in sections 3.2.1 and 3.2.2

[5]see section 1.3

in Table 3.3.

Table 3.3: A summary of the experimental work carried out at BARC-TIFR Pelletron accelerator facility

Experimental Details	Set 1	Set 2
Proton energies (MeV)	7, 15, 18.8	13, 16, 19, 22
neutron energies (MeV)	5.08, 12.47, 16.63	10.95, 13.97, 16.99, 20.00
Sample reactions	$^{159}Tb(n,\gamma)^{160}Tb$	^{113}In(n, n')^{113m}In
		^{115}In(n, n')^{115m}In
		^{115}In(n, 2n)^{114m}In
Monitor reactions	$^{232}Th(n,f)^{97}Zr$	$^{27}Al(n,\alpha)^{24}Na$
Sample thickness	2 mg/cm^2	0.025 mm
Monitor thickness	0.025 mm	0.1 mm
Sample weight	$\approx$ 33.3 mg	$\approx$ 186 mg
Monitor weight	$\approx$ 211 mg	$\approx$ 33 mg
Sample dimensions	$\approx 1 \times 0.5$ *cm*^{2}	1×1 *cm*^{2}
Monitor dimensions	$\approx 1 \times 0.5$ *cm*^{2}	1×1 *cm*^{2}

A complete description regarding the generation of neutrons from $^{nat}Li(p,n)$ reaction is provided in section 3.9. After stopping the irradiation, the irradiated sample were allowed to cool for a sufficient time interval. Then, each sample was separately mounted on separate perspex plates for the γ-ray spectrometry.
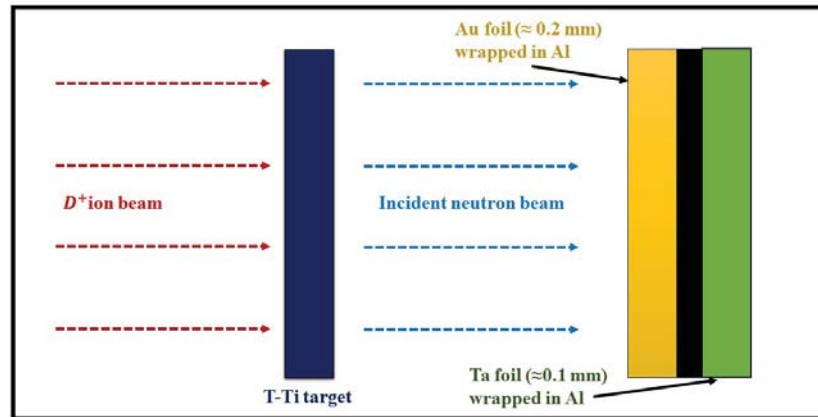

Figure 3.10: Schematic diagram showing the arrangements used for the neutron irradiation.

The γ-ray spectrometry was performed using a common HPGe detector setup coupled with a PC based γ-acquisition software[6]. During the counting to minimize summing errors (below 2%), the samples were kept at a convenient distance from the detector endcap. The detector system was pre-calibrated with a standard ^{152}Eu source [29] and the resolution of detector was measured to $\approx$ 1.88 keV for the 1.33 MeV γ-line of ^{60}Co.

---

[6]see section 3.4.1

In the experiments performed at purnima, the accelerated D^+ ions were impinged on TiT target to produce a suitable energy of neutrons. Metal target along with the monitor foil were separately wrapped in thin Al foil (≈ 0.011 mm thick). The prepared stack of target and monitor foil were placed at an angle of $0°$ with respect to the D^+ ion beam direction. A schematic diagram of the irradiation setup is shown in Figure 3.10.

At 99.71 keV accelerated D^+ ions were impinged onto TiT target to produce neutrons. The neutron beams of 14.78 MeV energy through DT reaction were then used for the sample irradiation. After sufficient amount of irradiation the samples were cooled to keep the radiation dose as low as possible. The samples were then separately counted by using a HPGe detector. Detail of the irradiated samples with the monitors used at Purnima experimental facility is provided in Table 3.4.

Table 3.4: A summary of the experimental work carried out at BARC-Purnima accelerator facility

tails	Set 1
D^+ ion current	300 kV
neutron energy	14.78
Sample reactions	^{181}Ta(n, 2n)^{180}Ta
Monitor reactions	^{197}Au(n, 2n)^{196}Au
Sample thickness	0.025 mm
Monitor thickness	0.025 mm
Sample weight	239.12 mg
Monitor weight	334.30 mg
Sample dimensions	1.1×1.1 cm^2
Monitor dimensions	1.1×1.1 cm^2

3.9 Estimation of Neutron Flux

Neutron beam was generated using ^{nat}Li target. When high energy protons are bombarded on a ^{nat}Li, they generate different nuclear reactions and some of it takes contributes in the outgoing neutron spectrum. Basically, the $^{nat}Li(p,n)$ reaction higher energies quasi-monoenergetic neutron spectrum, containing the lower energy neutron contribution with distinct broad peak. The natural Li target has two isotopes: ^6Li with an abundance of 7.42%, and ^7Li with 92.58% abundance [29]. Hence, the $^7Li(p,n)^7Be$ reaction has a threshold energy of 1.88 MeV in its ground state [43], making it the dominant channel that contributes to the outgoing spectrum. The neutron generated through this channel is mostly high energy, which makes the prominent peak at end point of spectrum (cut known as the n_0 group.). Secondly, for the reaction $^7Be^*$ the threshold at the first excited state is 2.38 MeV [43] which also contribute to the spectrum via

n_1 group of neutrons. Hence, the threshold of both groups comes within a few MeV region, therefore, at higher energy end of neutrons reflects distinct broad peak. Further, as the incident proton energy increases ($E_p \geq 2.4$ MeV), along with the $^7Li(p,n)^7Be$ reaction, many other channels such as, the $^7Li(p,\gamma)^8Be$ reaction, open at threshold above 3.23 MeV. Above 4.5 MeV, the fragmentation of ^8Be adds up more low energy neutrons towards the tail region of the spectrum. As the energy further increase, more and more breakup channels contribute and the neutron spectrum lengthens into a continuum of low energy neutrons below 4 MeV incident proton energies.
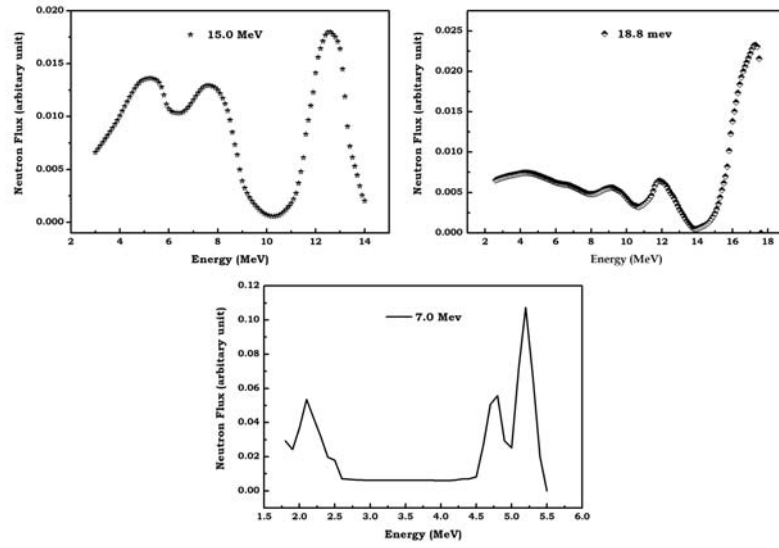
Figure 3.11: Typical neutron fluxes used for the present measurements reproduced by using the liturature data [74]

Scaling and interpolation was done wherever necessary to keep the threshold for all the neutron at $E_p - 1.88$ MeV. The neutron spectrum for energies within 5-22 MeV are given in Figures 3.11 and 3.12. These neutron spectra have been used by different groups [37, 44, 45] for similar reaction cross-section studies. To determine the neutron flux we combine the neutron flux with each of the theoretical cross-sections accumulated either from TALYS [46] or from the evaluated data libraries like ENDF/B-VII.1 [47]. The following equation is used to determine the weighted average cross-section σ_W of the monitor reaction,

$$< \sigma_W >= \frac{\Sigma_{E_j}\phi_j\sigma_j}{\Sigma_{E_j}\phi_j} \tag{3.42}$$

where, σ_j is the reaction cross-section for monitor and ϕ_j is the neutron flux at energies E_j. Equation 3.42 is a discrete form of equation 3.14,

$$< \sigma_W >= \frac{\int_{E_j}\phi_{E_j}\sigma_{E_j}}{\int_{E_j}\phi_{E_j}}. \tag{3.43}$$
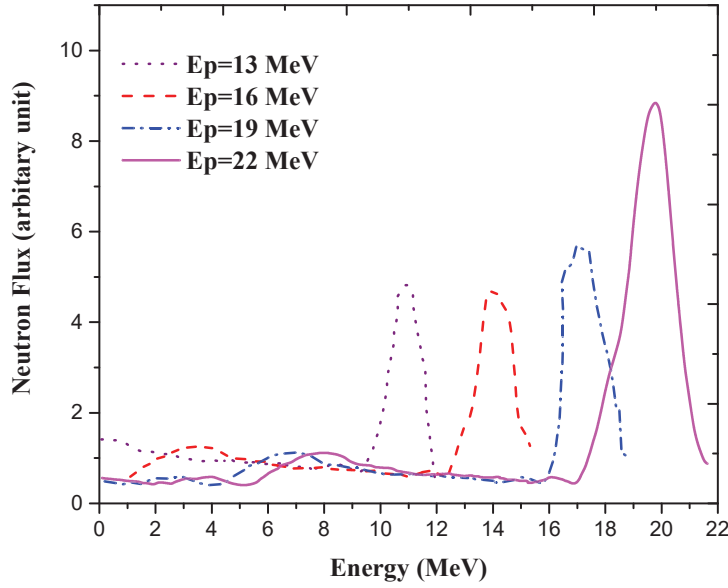
Figure 3.12: Neutron spectra generated from ^{nat}Li(p,n) reaction using 13, 16, 19 and 22 MeV protons

This value of σ_W is used in equation 3.13 to determine the neutron flux for the specific irradiation. After determining flux, the cross-section for particular reaction were calculated from the final equation 3.15.

3.10 Data Analysis for the $^{159}Tb(n,\gamma)^{160}Tb$, $^{113}In(n,n')^{113m}In$, $^{115}In(n,2n)^{114m}In$, $^{115}In(n,n')^{115m}In$, and $^{181}Ta(n,2n)^{180}Ta$ reactions

In the present work, the $^{159}Tb(n,\gamma)^{160}Tb$ [18], $^{113}In(n,n')^{113m}In$, $^{115}In(n,2n)^{114m}In$, $^{115}In(n,n')^{115m}In$ [19], and $^{181}Ta(n,2n)^{180}Ta$ [20] reaction cross-section were measured within 5-20 MeV incident neutron energies. The proton beams of 7-22 MeV were used for the production of the neutrons of different energies using $^{7}Li(p,n)$ neutron generator reaction at TIFR-BARC. Whereas the D^{+} ion beam from a RF ion source (180 kv) were used for the production of the neutrons at around 14.78 MeV using $^{3}H(d,n)^{4}He$ reaction neutron source [7]. For both the measurements the neutron flux were measured with the help of the weighted average cross-sections of the specific monitor reactions. The cross-sections were determine by using the equation 3.15. The residues can be populated in the neutron induced reactions with $^{159}Tb(n,\gamma)^{160}Tb$, $^{113}In(n,n')^{113m}In$, $^{115}In(n,2n)^{114m}In$, $^{115}In(n,n')^{115m}In$, and $^{181}Ta(n,2n)^{180}Ta$ isotopes is listed in Table 3.5. The typically

---

[7]The $^{159}Tb(n,\gamma)^{160}Tb$ [18], $^{113}In(n,n')^{113m}In$, $^{115}In(n,2n)^{114m}In$, and $^{115}In(n,n')^{115m}In$ [19], reactions were study at BATC-TIFR, whereas the $^{181}Ta(n,2n)^{180}Ta$ [18] reaction cross-section investigated at BARC PURNIMA

Table 3.5: Nuclear spectroscopic data for the isotopes used in the measurement of the $^{232}Th(n,\gamma)$, $^{100}Mo(n,2n)$ and $^{58}Ni(n,x)$ reaction cross-sections. The data are taken from the NuDat [29], Q-value calculator and Q-tool [43] data library.

Reaction	Threshold (Q-value) (MeV)	$T_{1/2}$	Decay Mode (%)	E_γ (keV)	I_γ (%)
$^{159}Tb(n,\gamma)^{160}Tb$	—	16.749 ± 0.008 h	β^- (100)	298.578 ± 0.017	26.1 ± 0.6
				879.378 ± 0.002	30.1 ± 0.6
				1177.954 ± 0.003	14.9 ± 0.3
$^{232}Th(n,f)^{97}Zr$ (m)	—	16.749 ± 0.008 h	β^- (100)	743.36 ± 0.03	93.09 ± 0.01
$^{113}In(n,n')^{113m}In$	—	1.65 ± 0.04 h	IT (100%)	391.69 ± 0.03	64.94 ± 0.17
$^{115}In(n,2n)^{114m}In$	9.117 (0.3)	49.51 ± 0.01 d	IT (96.75%)	190.27 ± 0.03	15.56 ± 0.15
			ε (3.25%)		
$^{115}In(n,n')^{115m}In$	—	4.48 ± 0.04 h	IT (95.00%)	336.24 ± 0.25	45.90 ± 0.01
			β^- (5.00%)		
$^{27}Al(n,\alpha)^{24}Na$ (m)	3.249 (0.05)	14.99 ± 0.12 h	β^- (100%)	1368.62 ± 0.05	89.43 ± 0.23
$^{181}Ta(n,2n)^{180}Ta$	7.618 (1.3)	8.154 ± 0.296 h	ε (85%)	93.32 ± 0.02	4.5 ± 0.4
			β^- (15%)		
$^{197}Au(n,2n)^{196}Au$ (m)	—	6.1669 ± 0.0006 d	ε (93%)	355.71 ± 0.06	87 ± 3
			β^- (7%)		

(m) $\rightarrow$ monitor reaction, $h \rightarrow hour$, $d \rightarrow day$,

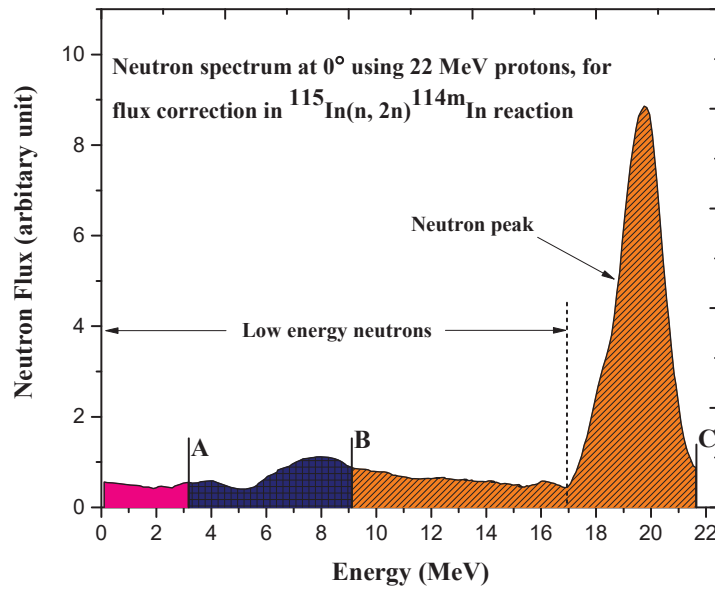**Figure 3.13:** Neutron flux correction for the threshold energy reactions where $^{27}Al(n, \alpha)^{24}Na$ reaction has threshold energy of 3.24 MeV labeled as A and $^{115}In(n, 2n)^{114m}In$ reaction has threshold energy 9.11 MeV labeled as B and maximum neutron energy labeled as C

recorded γ-ray spectra for all the sample/monitor reactions are also given in the Figures 3.14, 3.15, and 3.16, respectively for Tb, In and Ta isotopes.

3.11 Excitation Function of the $^{159}Tb(n, \gamma)^{160}Tb$ Reaction

In the present work, the final corrected $^{159}Tb(n, \gamma)^{160}Tb$ reaction cross sections at the spectrum average peak neutron energies of 5.08 ± 0.16, 12.47 ± 0.82, and 16.63 ± 0.95 MeV respectively, are given in Table 3.6 and plotted in 3.17. These cross-sections are significant to improve the nuclear database and also crucial in the reactor design. For the validation of the present measured experimental data, the standard nuclear model plays a vital role. We can observe from Figure 3.17 that, the reaction cross-sections measured in the present work are in agreement with the predicted data using theoretical code TALYS 1.9 as well as with literature data [48–53]. Different level density models were tested for the reproduction of the present and the literature data from EXFOR. Among those, ldmodel 1, which accounts for the constant temperature Fermi gas model [54] have been found to be successful in the reproduction of cross-sections. However, the present data points were found consistent with the Ld model 4 predictions. The data were also compared with those from ENDF/BVII.1 and JENDL-4.0 libraries. However, the present data at 5.08 ± 0.16 MeV is significantly lower than the literature data. It may also be observed that this cross-section value agrees with data
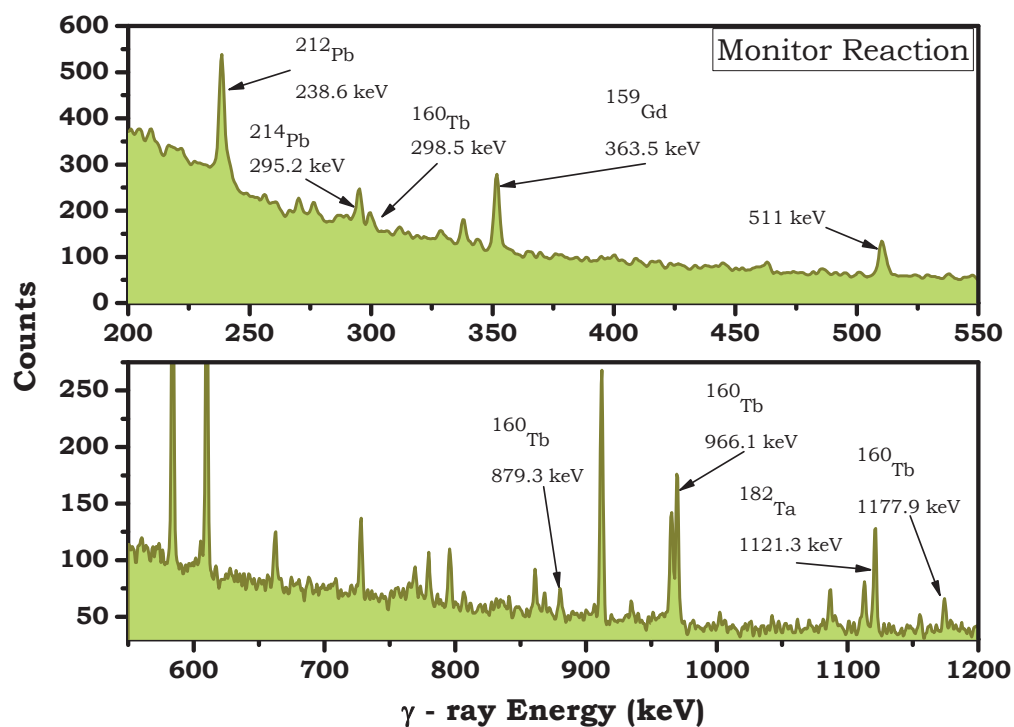
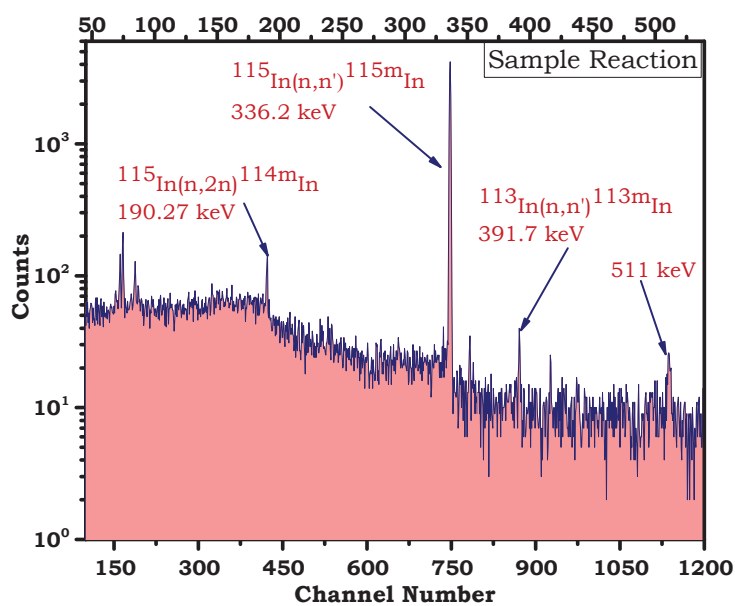**Figure 3.14:** Typically recorded γ-ray spectrum for the Terbium sample

Figure 3.15: Typically recorded γ-ray spectrum for the Indium sample
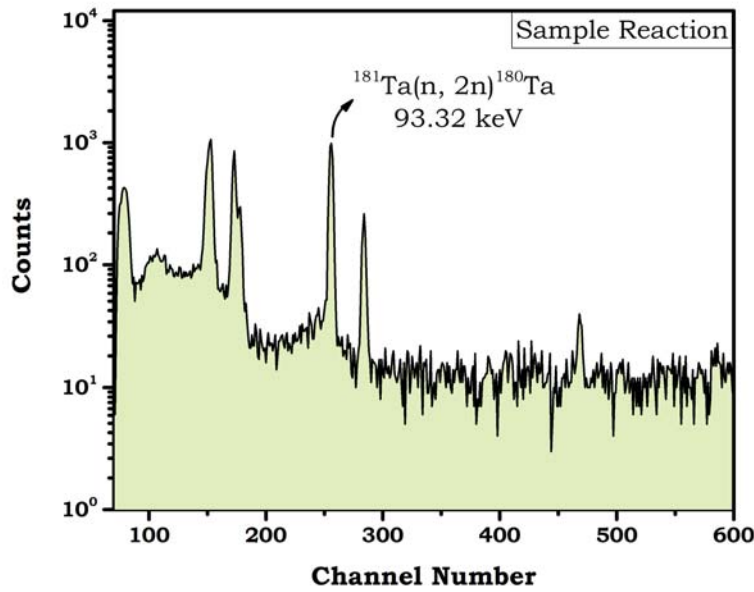
Figure 3.16: Typically recorded γ-ray spectrum for the Tantalum sample

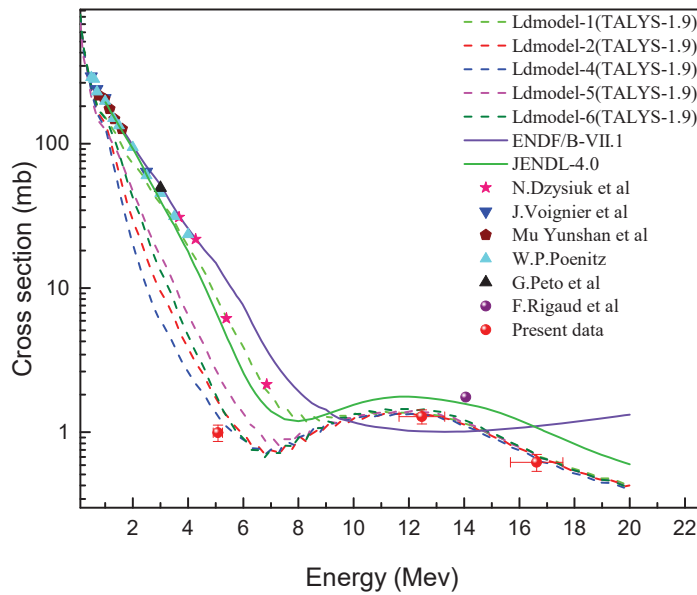**Figure 3.17:** Comparison of the experimentally measured $^{159}Tb(n,\gamma)^{160}Tb$ reaction cross-section with literature data and the theoretical model codes

predicted by ldmodel 4 of the theoretical code TALYS 1.9. It suggests that more experimental data are needed to be obtained and compared with the different nuclear models. Since the measured cross-sections are correlated with each other, therefore, a detailed covariance analysis have also been carried out in order to find out the exact values of the uncertainties in the measured data.

Covariance analysis is a well-known method which can be used to calculate the uncertainty in the measured data by propagating the error in each quantity used in the measurement.

Table 3.6: ^{159}Tb(n, γ) reaction cross-section at different spectrum average peak neutron energies.

Neutron Energy (MeV)	Measured Cross-Section (mb)	Tailing part		Corrected Cross-Section (mb)
		ENDF-B/VII.1	JENDL-4.0	
16.63 ± 0.95	0.630 ± 0.082	0.013	0.010	0.618 ± 0.082
5.08 ± 0.16	1.002 ± 0.129	0.011	0.008	0.993 ± 0.129
12.47 ± 0.82	0.074 ± 0.145	0.074	0.574	1.285 ± 0.145

3.11.1   Theoretical analysis with TALYS-1.9

The theoretical calculations have been done to reproduce the measured cross-section by using a recent version of standard nuclear reaction modal code, TALYS-1.9 [46]. The code is used extensively for nuclear data prediction for the emission of the γ,neutron, proton, triton and other particles, by using the reaction parameter from the Reference Input Parameter Library [55]. The code deals with the effect of level density parameters on the compound nucleus, pre-equilibrium, and direct reaction mechanisms as a function of incident particle energy. Koning and Delaroche proposed the optical model parameters by using a global potential. By using the Hauser-Feshbach model, the compound reaction mechanism was incorporated [56]. The pre-equilibrium contribution has been incorporated into the exciton model developed by Kalbach. In the present work, the calculations have been done by considering all the parameters of the code as default like deformation, resonance, γ-ray, optical model, fission, and level density (lD) models. The comparison of theoretically predicted and EXFOR data with the present experimental results.

3.12   Excitation Function of the $^{113}In(n,n')^{113m}In$, $^{115}In(n,2n)$ ^{114m}In, $^{115}In(n,n')^{115m}In$ Reactions

The excitation function of the $^{113}In(n,n')^{113m}In$, $^{115}In(n,2n)^{114m}In$, $^{115}In(n,n')^{115m}In$ reactions were measured at average neutron energies of 10.95 ± 0.67, 13.97 ± 0.97, 16.99 ± 0.88, and 20.00 ± 0.94 MeV relative to $^{27}Al(n,\alpha)$ monitor reaction as shown in Table 4.2. The uncertainties in the corrected cross-sections were calculated with covariance analysis and were found to be in the range of 4 – 19%. The tailing corrected cross-sections with uncertainties are listed in Table 4.2 for all the three reactions, however, the detailed calculations for generating covariance

matrices for efficiency of the detector used and cross-sections are given in Appendix A. The present results were compared with the literature data [4, 57–78], theoretical model predictions from TALYS-1.9 [46] code using available input level density parameters and evaluated data library JENDL-4.0 [79]. Among the three reactions, the first and third were measured at neutron energies 10.95 ± 0.67, 13.97 ± 0.97, 16.99 ± 0.88, and 20.00 ± 0.94 MeV, whereas the second-one measured at neutron energies 13.97 ± 0.97, 16.99 ± 0.88, and 20.00 ± 0.94 MeV. The results are plotted in the Figures 3.18-3.20. It can be observed from the Figure 3.18 that the present results are in agreement with the literature data [4, 57–78]. The present data gives a satisfactory agreement with the findings of previous measurements. Mainly, literature reported the uncertainty in cross-sections by pursuing traditional method by taking the quadratic sum of systematic and statistical errors, which do not consider the uncertainties of the monitor data. Whereas the present study shows the importance of detailed error analysis for the neutron data. The determined cross-sections largely based on monitor data, which can be calculated from covariance method.
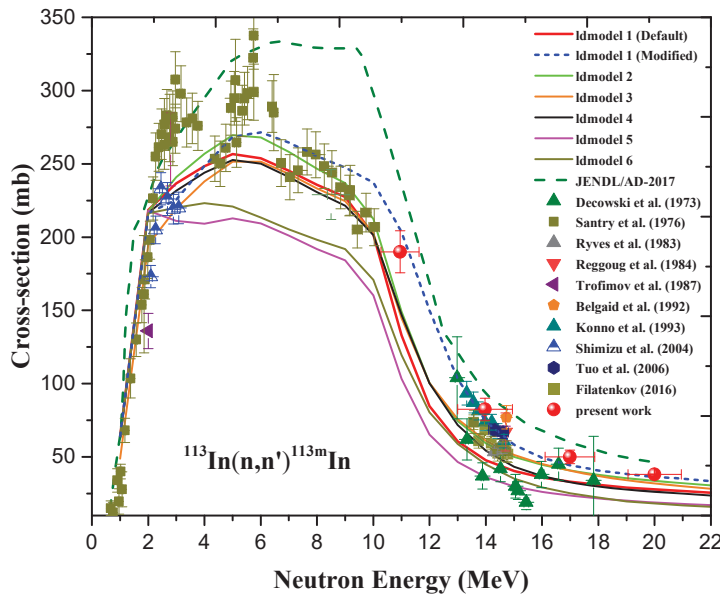

Figure 3.18: The experimentally measured ^{113}In(n, n')^{113m}In reaction cross-section compared with the literature data [4, 57–66], and theoretical nuclear models of TALYS-1.9 The default value of ldmodel 1 have been chosen to fit the present and previous data.

Table 3.7: Measured and tailing corrected cross-sections for the ^{113}In(n, n')^{113m}In ^{115}In(n, 2n)^{114m}In ^{115}In(n, n')^{115m}In reactions.

Neutron energy (MeV)	Neutron flux ($ncm^{-2}s^{-1}$)	^{113}In(n, n')^{113m}In reaction cross-section (mb)		
		Measured	Tailing correction	Final
10.95 ± 0.67	5.72 x 10^6	360.28	171.23	189.05 ± 14
13.97 ± 0.97	2.46 x 10^6	120.84	39.33	81.51 ± 08
16.99 ± 0.88	1.83 x 10^6	70.27	19.04	51.23 ± 05
20.00 ± 0.94	8.53 x 10^6	54.26	16.41	37.85 ± 04

Neutron energy (MeV)	Neutron flux ($ncm^{-2}s^{-1}$)	^{115}In(n, 2n)^{114m}In reaction cross-section (mb)		
		Measured	Tailing from [46]	Final
13.97 ± 0.97	2.46 x 10^6	1740.35	495.05	1245.30 ± 12
16.99 ± 0.88	1.83 x 10^6	1783.49	559.49	1224.00 ± 17
20.00 ± 0.94	8.53 x 10^6	971.26	288.28	682.98 ± 19

Neutron energy (MeV)	Neutron flux ($ncm^{-2}s^{-1}$)	^{115}In(n, n')^{115m}In reaction cross-section (mb)		
		Measured	Tailing from [46]	Final
10.95 ± 0.67	5.72 x 10^6	377.71	166.63	211.08 ± 10
13.97 ± 0.97	2.46 x 10^6	137.27	52.15	85.12 ± 06
16.99 ± 0.88	1.83 x 10^6	83.01	20.62	62.39 ± 04
20.00 ± 0.94	8.53 x 10^6	75.63	18.08	57.55 ± 04

It can also be observed from the Figure 3.18 that, the literature data are mostly concentrated below 6 MeV [57, 58, 66] and around 14 MeV [59–65], although minor discrepancies are observed in these data. Among the different level density models of TALYS-1.9 code [46], ldmodel 1 [80] and 4 [81] were found suitable to reproduce the reaction cross-section data to some extent, as compared to under-predicted results from the rest of the ldmodels. The ldmodel, based on the Constant Temperature model (CTM) effective, was used to modify the parameters given in equations (18) and (20), to achieve a better fit to the literature and the present data. The optimized parameter set of the CTM effective gas model is given in Table 3.8 and described in upcoming section 3.12.2 .

The measured cross-sections for ^{115}In(n, 2n)^{114m}In reaction are shown in Fig. 3.19. It is clear from the figure that, the (n, 2n) channel certainly contains larger discrepancies with significant uncertainties in the literature data [65, 69–71, 82] as compared to the previous case. A general disagreement is observed between the reported cross-sections from, Paulsen et al., [70] and others [60, 64, 72]. However, the present results follow the trend of the literature data reported by Wei et al., [71], Iwasaki et al., [72], and Filatenkov [65]. The present data also offer minimal uncertainties as compared to the literature data. The ldmodels present

in TALYS-1.9 [46], have been found to be successful in order to fit the ^{115}In(n, 2n)^{114m}In reaction cross-section data as seen in Fig. 3.19. The present data at 20 MeV is not following the trend as predicted by the theoretical values; however, the other data points from the present measurement follow the TALYS-1.9 code [46] results. Among the different ldmodels of TALYS-1.9 code [46], the CTM effective gas model was optimized to get a better agreement with the literature data. Table 3.8 gives the modified parameters used in Fig. 3.19.
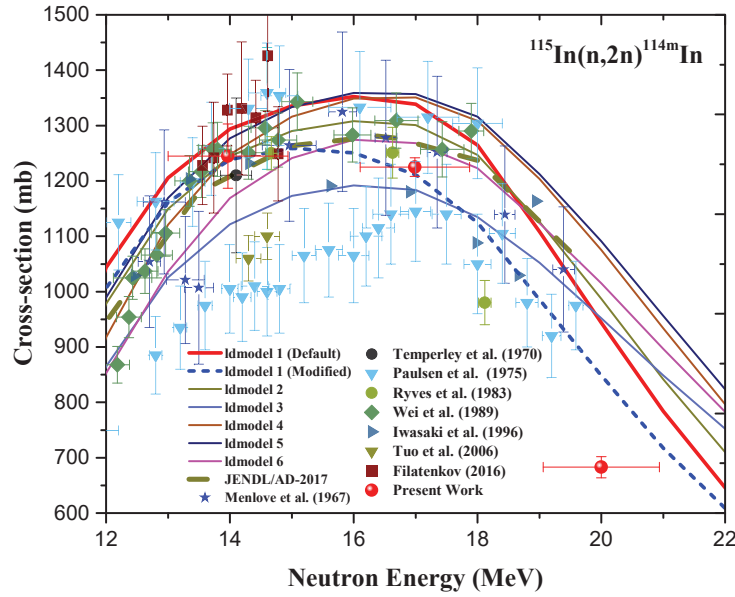

Figure 3.19: The experimentally measured ^{115}In(n, 2n)^{114m}In reaction cross-section compared with the literature data [60, 64, 65, 67–72], and theoretical nuclear models of TALYS-1.9 The default value of ldmodel 1 have been chosen to fit the present and previous data.

The present results of the ^{115}In(n, n')^{115m}In reaction, compared with the available literature [60, 63, 64, 67–69, 73–78] and the theoretical data from TALYS-1.9 [46] are shown in Fig. 3.20. It can be observed from the figure that, the present results are in decent agreement with those available in the literature [64,69,78,82]. The theoretical results from different ldmodels 1-6 show a general agreement upto 2 MeV. However, beyond that, only the ldmodel 2 [83, 84] based on the BFM successfully reproduces the data with minor under prediction within 2-6 MeV range. The ldmodels 1 and 3-6 under-predict the cross-section data beyond 2 MeV neutron energies. The parameter set of the ldmodel 2 [83, 84] is further improved to fit the cross-section data more accurately, as seen from Fig. 3.20. The optimized parameters for BFM are tabulated in Table 3.8.
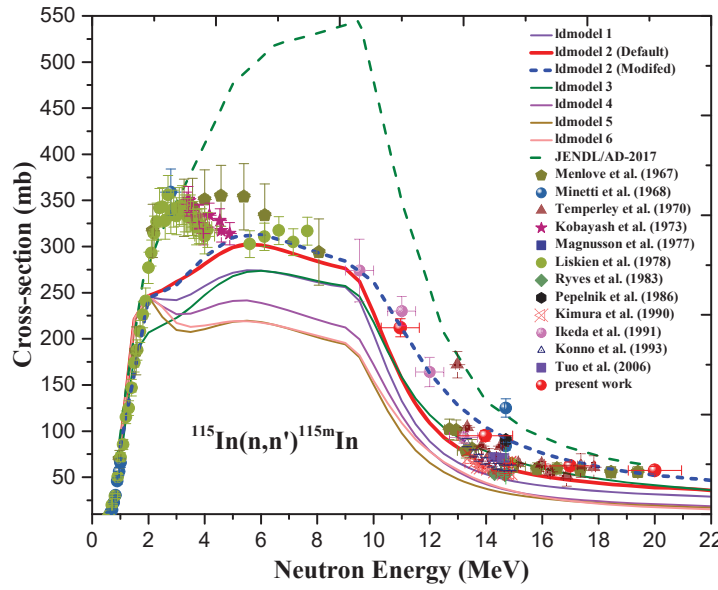
Figure 3.20: The experimentally measured $^{115}In(n, n')^{115m}In$ reaction cross-section compared with the literature data [60, 63, 64, 67–69, 73–78], and theoretical nuclear models of TALYS-1.9 The default value of ldmodel 2 have been chosen to fit the present and previous data.

3.12.1 $^{nat}Li(p,n)$ **spectrum production using MCNP code**

The neutron spectra at the proton energies 13, 16, 19, and 22 MeV were generated by using MCNP simulation code. The input file of the simulation code consists of cell, surface, source and tally cards. As shown in Figure 3.21, stack of Ta–Li–Ta has been placed along the x-direction. In same direction the opening of proton source has been model. The source position, particle type, energy and direction were defined by POS, ERG, AXS, DIR and PAR in SDEF card.For the better understanding, emitted protons from the source are illustrated in the diagram with black arrows. Whereas, once the proton beam passes through the Ta foil and interact with Li foil. During the interaction, neutrons are produced from one of the Li(p, n) reactions and Ta foil behind, most of the proton beam and only allows neutrons to get through (indicated with white arrows in Figure 3.21). These neutrons were recorded in the detector by using Tally F4 average flux in a cell and tally energy (En).

3.12.2 **Theoretical Calculation within the Framework of TALYS-1.9 code**

TALYS is the simulation code, which works as an interplay between the experimental and theoretical predictions. These theoretical predictions are based on different nuclear reaction models and parameterization. TALYS-1.9 [46] code
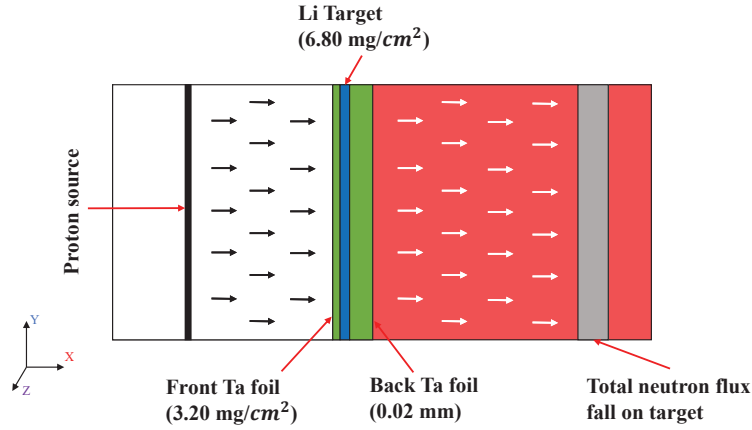
Figure 3.21: Geometry used to simulate the neutron spectrum by using MCNP [32] code

was used to predict the ^{113}In(n, n')^{113m}In, ^{115}In(n, 2n)^{114m}In and ^{115}In(n, n')^{115m}In reactions with default as well as modified parameter values in level density. In TALYS-1.9 [46] code, six level densities models are available, which can be analytically derived from microscopic models, which are described elsewhere [85]. In order to obtain the default values of the level density, all possible channels for neutron induced reactions have been considered. We have considered ld-model 1 [80] for, the ^{113}In(n, n')^{113m}In and ^{115}In(n, 2n)^{114m}In reactions and ldmodel 2 [83, 84] for the ^{115}In(n, n')^{115m}In reaction. The default parameters have not been able to produce the results satisfactorily, therefore, the ldmodel parameters have been adjusted to find a better agreement between the experimental and literature data.

The level density ρ depends on excitation energy E_x, spin state (J) and parity (Π) of the nucleus. Therefore, the number of nuclear levels per MeV are described by $\rho(E_x, J, \Pi)$. The total level density related to the total number of levels per MeV around E_x have been obtained by summing the level density over spin and parity as shown in Eq. (15).

$$\rho^{tot}(E_x) = \sum_J \sum_\Pi \rho(E_x, J, \Pi). \tag{15}$$

Since, the nuclear levels are degenerate in magnetic quantum number (M), Eq. (15) is modified with introducing of (2J+1) term is the level density. Then Eq. (15) can be rewritten as below,

$$\omega^{tot}(E_x) = (2J + 1) \sum_J \sum_\Pi \rho(E_x, J, \Pi). \tag{16}$$

Now, the final analytical expression of the level density in terms of $P(E_x, J, \Pi)$ parity distribution and $R(E_x, J)$ spin distribution $R(E_x, J)$ can factorized as follows,

$$\rho^{tot}(E_x, J, \Pi) = P(E_x, J, \Pi)R(E_x, J)\rho(E_x, J). \tag{17}$$

In the above equation the level density parameter (a) plays an important role. The energy dependent level density parameter (a) is given as

$$a(E_x) = \tilde{a}\left[1 + \delta\varepsilon_0\left(\frac{1 - e^{-\gamma U}}{U}\right)\right]. \tag{18}$$

where U is defined as in Eq. (19), where, Δ is an empirical parameter which gives energy shift and is included in the formula to simulate the known odd-even effect in the nuclei.

$$U = E_x - \Delta. \tag{19}$$

In Eq. 18 $\tilde{a}$ is the asymptotic value of level density (in the absence of shell effects), γ is the damping parameter ($\gamma = \frac{\gamma_1}{A^{\frac{1}{3}}} + \gamma_2$ used to determine when $a(E_x)$ approaches to $\tilde{a}$) and $\delta\varepsilon_0$ is the shell correction energy. In a phenomenological manner, the level density parameter shows the appearance of shell effect at low energy which disappears at higher energy. Hence, corresponding asymptotic value $\tilde{a}$ can be defined in the following manner;

$$\tilde{a} = \alpha A + \beta A^{2/3}, \tag{20}$$

where, A is the mass number, and α, and β are global density parameters that have been determined to give the best description of average level density over a whole range of nuclides [46]. The default and adjusted value of global density parameters of TALYS-1.9 [46] were used to compare the present work, and are given in Table 3.8. The first two reactions were compared with ldmodel 1, which is based on the Constant Temperature Fermi-Gas model (CTFGM). In the same level density model CTM is used in the low excitation energy region whereas, FGM is used in high excitation energy region. The transition from CTM to FGM is around the neutron separation energy [86]. On the other hand, the ^{115}In(n, n') reaction is compared with ldmodel 2 (based on Back-shifted Fermi gas model (BFM)). The ^{113}In(n, n'), ^{115}In(n, 2n) and ^{115}In(n, n') reaction cross-sections are obtained from TALYS-1.9 by default and adjusted parameters are plotted as in Figs 3.18-3.20. It is clear that, the theoretical cross-sections data from adjusted parameter in TALYS-1.9 are in decent agreement with the literature and measured data. The result of all the three reactions as shown in Figs 3.18-3.20, the calculated TALYS-1.9 gives a satisfactory agreement in the entire energy span of 1-22 MeV.

Table 3.8: Default and adjused parmeters used in the TALYS-1.9 calculations.

parameter	CTM		CTM		BFM	
	Default value	Adjusted value for ^{113}In(n, n′)	Default value	Adjusted value for ^{115}In(n, 2n)	Default value	Adjusted value for ^{115}In(n, n′)
α	0.06925	0.06925	0.06925	0.06925	0.07223	0.12239
β	0.28276	0.48562	0.28276	0.28276	0.19526	0.19526
γ_1	0.43309	0.73309	0.43309	0.33309	0.41028	0.11208

3.13   Excitation Function of $^{181}Ta(n, 2n)^{180}Ta$ Reaction Cross-sections around 14.78 MeV

The excitation functions of the $^{181}Ta(n, 2n)^{180}Ta$ reaction was determined at average neutron energy of 14.78 ± 0.20 MeV relative to the $^{197}Au(n, \gamma)196Au$ monitor reaction. The uncertainty in the present measurement calculated with the help of covariance analysis was found to be ≈ 15%.

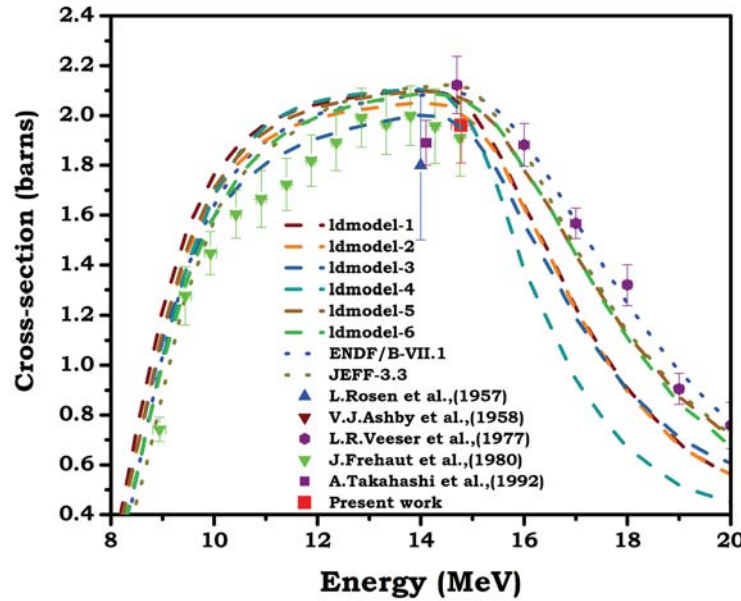**Figure 3.22:** Excitation function of $^{181}Ta(n, 2n)^{180}Ta$ reaction. A comparison of present data with the literature data [13–15,87,88] and the theoretical predictions using the TALYS-1.9 [46] code.

The cross-sections of the $^{181}Ta(n, 2n)^{180}Ta$ reaction was obtained as 1.83±0.15 barns. The present results were compared with the literature data [13–15, 87, 88], theoretical model predictions from TALYS-1.9 [46] code using different level density model available in it, ENDF/B-VII.1 [47], and JEFF-3.3 [89], evaluated data libraries. The results are plotted in the Figure 3.22. The excitation function

of the $^{181}Ta(n,2n)^{180}Ta$ reaction is shown in Figure 3.22. It can be examined from the figure that, the present result at the neutron energy of 14.78 ± 0.20 MeV is in excellent agreement with ldmodel three which is a generalized superfluid model of the TALYS-1.9 [46] and in close agreement with the previous experimental data of J. Frehaut et al. [14]. However, the prediction of the L.R. Veeser et al., [87], as well as evaluated from JEFF-3.3 [89], and ENDF/B-VII.1 [47] libraries are slightly higher. It suggests that more experimental data are needed to be obtained and compared with the different nuclear models.

✠ ✠ ✠ ✠

Bibliography

[1] Extending the global reach of nuclear energy through Thorium, Published by S.K. Malhotra, Head, Public Awareness Division, D.A.E, Govt. of. India, September 2008, `http://dae.nic.in/writereaddata/.pdf_38`.

[2] C. Rubbia, J.A. Rubio, et al., Conceptual Design Of a Fast Neutron Operated High Power Energy Amplifier,CERN Report No. CERN/AT/95-44 (ET) (1995).

[3] C.D. Bowman, et al., Nuclear Energy Generation and Waste Transmutation Using an Accelerator-Driven Intense Thermal Neutron Source, Los Alamos National Laboratory Report LA-UR-91-2601 (1991).

[4] C.D. Bowman, *Ann. Rev. Nucl. Part. Sci.* **48**; (1998) 505.

[5] F. Carminati, R. Klapisch, et al., An Energy Amplifier for Cleaner and Inexhaustible Nuclear Energy Production Driven by Particle Beam Accelerator, CERN Report No. CERN/AT/93-47 (ET) (1993).

[6] E.D. Arthur, S.A. Schriber, A. Rodriguez(Editors), The International Conference on Accelerator-Driven Transmutation Technologies and Applications, Las Vegas, Nevada, USA, 1994, AIP Conf. Proc., Vol. **346**; (1995).

[7] Accelerator Driven Systems: Energy Generation and Transmutation of Nuclear Waste, Status report: IAEA TECDOC-985 (1997).

[8] S. Ganesan, *Pramana J. Phys.* **68**; (2007) 257.

[9] A.J. Koning, J. Blomgren, Nuclear data for sustainable nuclear energy, JRC Scientific and Technical Report No. EUR23977EN-2009, (2009) retrieved from ⟨https:// cordis.europa.eu/pub/fp6-euratom/docs/candidefinal-report en.pdf⟩.

[10] D.A. Petti, Silver-indium-cadmium control rod behavior and aerosol formation in severe reactor accidents (1987).

[11] H.A. Grench, H.O. Menlove, *Phys. Rev.*, **165**; (1968) 1298.

[12] H. Lu, W. Ke, et al., *Chin. J. Nucl. Phys.*, **11**; (1989) 53.

[13] A. Takahashi, Y. Sasaki, and H. Sugimoto, International Atomic Energy Agency (1989).

[14] J. Frehaut, A. Bertin, R. Bois, and J. Jary, CEA Centre d'Etudes de Bruyeres-le-Chatel (1980).

[15] L. Rosen, and L. Stewart, *Physical Review*, **107**; 3 (1957) 824.

[16] U. Fischer, P. Batistoni, et al., *Proc. International conference on nuclear data for science and technology* vol **769**; (AIP Conf.) (2005) 1478.

[17] Y. Takahashi et al., *Japan. Nucl. Fusion*, **51**; (113015) (2011) 11.

[18] B.K. Soni, R. Makwana, et al., *App. Rad. Iso.* **141**; (2018) 10-14.

[19] B. Soni, S. parashari, et al., "Measurement of (n, xn) reaction cross-sections on $^{113,115}In$ isotopes using quasi-monoenergetic neutrons within 10-20 MeV", *Eur. Phys. Jour. P* **135**; (2019) 300.

[20] B.K. Soni, S. Parashari, et. al., *Indi. Jou.of Pure & App. Phy.* **58**; (2020) 228-233.

[21] Siddharth Parashari, *Study of nuclear reaction cross sections for reactor applications*, Department of Physics, The Maharaja Sayajirao University of Baroda, (2019) http://hdl.handle.net/10603/329685.

[22] A. Sinha, T. Roy, et al., *Nuc. Ins. and Met. in Phy. Res. B*, **350**; (2015) 66-70.

[23] T. Patel, S. Bisnoi et al., *Proc. 18th NSRP-2009*, M. L. S University, Udaipur, Rajasthan, India.

[24] S. Bisnoi, T. Patel, et al., *Proc. of the DAE symp. on Nucl. Phys.*, **56**; (2011)

[25] S. Mukherjee, B. Bindu Kumar, et al., **Phys. Rev. C**, **55**; (1997) 2556.

[26] J. Acharya, S. Mukherjee, et al., *Phys. Rev. C*, **93**; (2016) 024608 .

[27] G.F. Knoll, Radiation Detection and Measurement 3 rd edition (**Chapters 12 and 13**), John Wiley & Sons, (1999).

[28] HPGe Detector Manufacturing, ORTEC, `http://www.ortec-online.com`.

[29] NuDat 2.7β 2011, *National Nuclear Data Center, Brookhaven National Laboratory*, `http://www.nndc.bnl.gov/`.

[30] MAESTRO Multichannel Analyzer Emulation Software, ORTEC, `https://www.ortec-online.com/products/application-software/maestro-mca`

[31] Genie 2000 Gamma Analysis Software, MIRION Technologies, `https://www.mirion.com/products/genie-2000-gamma-analysis-software`.

[32] LAMPS:Linux Advanced MultiParameter System, https://www.tifr.res.in/ pell/lamps.html

[33] FitzPeaks Gamma Analysis and Calibration Software, Jim Fitzgerald, JF Computing Services, STANFORD IN THE VALE, Oxfordshire, SN78LE, `https://www.jimfitz.co.uk/fitzpeak.htm`.

[34] Thomas M. Semkow, Ghazala Mehmood, et al., *Nucl. Inst. and Meth. in Phys. Res. A*, **290**; (2) (1990), 437.

[35] T. Vidmar, G. Kanish, et al., *Appl. Rad. Isot.*, **69**; (2011) 908.

[36] R.C. Kotch, Activation Analysis Hand Book, Academic Press, New York and London, (1960).

[37] B.S. Shivashankar, H. Naik, et al., *Nucl. Sci. and Eng.*, **179**; (2015) 423. DOI: 10.13182/NSE14-19.

[38] N. Otuka, B. Lalremruata, et al., *Radiat. Phys. Chem.*, **502**; (2017) 140.

[39] T.M. Semkow, Ghazala Mehmood, et al., *Nucl. Inst. and Meth. in Phys. Res. A*, **290**; (2) (1990) 437.

[40] Y. Santhi Sheela, *Covariance analysis in neutron activation measurements of ^{59}co (n,2n) ^{58}co and ^{59}co (n,γ) ^{60}co reactions in the mev region*, Department of Statistics, Manipal University (2018) http://hdl.handle.net/10603/209015.

[41] L.P. Geraldo and D. Smith, *Nuclear Instruments and Methods in Physics Research A*, **290**; (1990) 449.

[42] W. Mannhart, INDC(NDS)-0588 Rev., International Atomic Energy Agency (2013).

[43] Qtool: calculation of reaction Q-values and threshold, Los Alamos National Library, `http://cdfe.sinp.msu.ru/services/calc_thr/calc_thr.html`.

[44] B.S. Shivashankar H. Naik, et al., *Jour. of Radioanalytical and Nuclear Chemistry*, **292**; (2012) 745. DOI: 10.1007/s10967-012-1646-9.

[45] M. Bhike, A. Saxena, et al., *conf. Nucl. Data for Adv. Nucl. Systems*, Mangalore, India, 2006, p.(TP15) (2006).

[46] A. J. Koning, S. Hilaire, et al., *TALYS user manual, A nuclear reaction program, NRG-1755 ZG PETTEN*, The Netherlands (2015).

[47] ENDF/B-VII.1, 2011, National Nuclear Data Center, Brookhaven National Laboratory,`http://www.nndc.bnl.gov/exfor/endf00.jsp`.

[48] Dzysiuk, N., Kadenko, I., Gressier, V., Koning, A.J., 2015. Cross section measurement of the 159Tb(n, γ)Tb160 nuclear reaction. Nucl. Phys. A 936, 6–16.

[49] Voignier, J., Joly, S., Grenier, G., 2017. Capture Cross Sections and Gamma-Ray Spectra from the Interaction of 0.5- to 3.0-MeV Neutrons with Nuclei in the Mass Range A = 45 to 238.

[50] Rigaud, F., Irigaray, J.L., Petit, G.Y., Saporetti, F., 1971. Spectra of high-energy photons following the capture of 14 MeV neutrons by 133Cs, 139La, Ce and 159Tb.

[51] Petö, G., Miligy, Z., Hunyadi, I., 1967. Radiative capture cross section for 3 MeV neutrons ⟨http://dx.doi.org/10.1016/0022-3107(67)90089-5⟩.

[52] Yunshan, Mu, Yexiang, Li, Shiming, Wang, Zhengyu, Xiang, Haishan, Xu, 1988. Measurements of the fast neutron radiative capture cross sections of natural Terbium and Hafnium. J: Chin. J. Nucl. Phys. (Beijing) 10 (3) (233 NSR: 1988 MU17).

[53] Poenitz, W.P., 1982. Conference: Argonne National Laboratory report series, Fast-Neutron Capture-Cross-Section Measurements With The Argonn National Laboratory Large- Liquid- Scintillator Tank, Vol. 4, No. 83, p. 239.

[54] Gilbert, A., Cameron, A.G.W., 1965. A composite nuclear-level density formula with shell corrections. Can. J. Phys. 43 (8), 1446–1496. https://doi.org/10.1139/p65-139.

[55] Capote, R., Herman, et al., 2009. RIPL – reference input parameter library for calculation of nuclear reactions and nuclear data evaluations. Nucl. Data Sheets 110, 3107–3214.

[56] Hauser, W., Feshbach, H., 1952. The inelastic scattering of neutrons. Phys. Rev. 87, 366.

[57] D. Santry, J. Butler, *Canadian Journal of Physics*, **54**; (1976) 757.

[58] Y.N. Trofimov, Yadernye Konstanty, USSR report to the I.N.D.C., **284**; (1987) 10.

[59] P. Decowski, W. Grochulski, et al., *Nuclear Physics A*, **204**, (1973) 121.

[60] T. Ryves, M. Hongchang, et al., *Journal of Physics G: Nuclear Physics*, **9**; (1983) 1549.

[61] A. Reggoug, G. Paić, A. Chiadli, Nuclear Data for Science and Technology, (1983) 873.

[62] M. Belgaid, M. Siad, et al., *Journal of Radioanalytical and Nuclear Chemistry*, **166**; (1992) 493.

[63] C. Konno, Y. Ikeda, et al., JAERI reports, **1329**; (1993).

[64] F. Tuo, F. Zhou, et al., *Applied Radiation and Isotopes*, **64**; (2006) 910.

[65] A. Filatenkov, INDC (CCP)-0460,(2016).

[66] T. Shimizu, H. Sakane, et al., *Annals of Nuclear Energy*, **31**; (2004) 1883.

[67] H.O. Menlove, K.L. Coop, et al., *Phys. Rev.*, **163**; (1967) 1308.

[68] B. Minetti, A. Pasquarelli, *Physik A Hadrons and nuclei*, **217**; (1968) 83.

[69] J.K. Temperley, D.E. Barnes, tech. rep., BALLISTIC RESEARCH LABS ABERDEEN PROVING GROUND MD, (1970).

[70] A. Paulsen, H. Liskien, et al., *Atomkernenergie*, **26**; (1975) 34.

[71] W. Ke, W. Zhao, et al., *Chinese Journal of Nuclear Physics*, **11**; (1989) 11.

[72] S. Iwasaki, T. Win, et al., Proc. JAERI, **21** (1996).

[73] K. Katsuhei, I. Kimura, et al., *Journal of Nuclear Energy*, **27**; (1973) 741.

[74] H. Liskien, F. Arnotte, et al., *Nuclear Science and Engineering*, **67**; (1978) 334.

[75] G. Magnusson, P. Andersson, et al., *Physica Scripta*, **21**; (1980) 21.

[76] R. Pepelnik, B. Anders, et al., Report, GKSS in "Progress Report on Nuclear Data Research in Germany 1984" (1985).

[77] I. Kimura, K. Kobayashi, *Nuclear Science and Engineering*, **106**; (1990) 332.

[78] Y. Ikeda, C. Konno, et al., *Nuclear Data for Science and Technology*, (1992) 294-296.

[79] K. Shibata, O. Iwamoto, et al., *J. Nucl. Sci. Technol.*, **48**; (2011).

[80] A. Gilbert, A. Cameron, *Canadian Journal of Physics*, **43**; (1965) 1446.

[81] R. Capote, M. Herman, et al., *Nuclear Data Sheets*, **110**; (2009) 3107.

[82] H.O. Menlove, K. Coop, et al., *Physical Review*, **163**; (1967) 1308.

[83] A. Ignatyuk, K. Istekov, et al., *Sov. J. Nucl. Phys.*, **29**; (1979).

[84] W. Dilg, W. Schantl, et al., *Nuclear Physics A*, **217**; (1973) 269.

[85] A.J. Koning, S. Hilaire, et al., *Nuclear Physics A*, **810**; (2008) 13.

[86] L.R.M Punte, B. Lalremruata, et al., *Phys. Rev. C*, **95**; (2017) 024619.

[87] L.R. Veeser, E.D. Arthur, P.G. and Young, *Physical Review C*, **16**; 5 (1977) 1792.

[88] V.J. Ashby, H.C. Catron, L.L. Newkirk, and C.J. Taylor, *Physical Review*, **111**; 2 (1958) 616.

[89] A.J. Koning, E. Bauge, et al., Status of the JEFF nuclear data library. *J. Kor. Phys. Soc.*, **59**; issue 2 (2011) 1057.